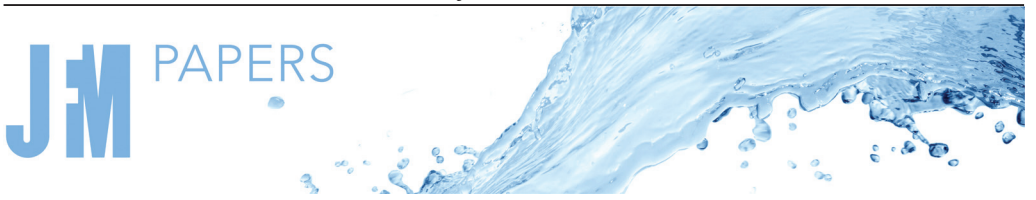
*J. Fluid Mech.* (2021), *vol*. 929, A20, doi:10.1017/jfm.2021.822



# Influence of nozzle external geometry on wavepackets in under-expanded supersonic impinging jets

**Shahram Karami**[1],† **and Julio Soria**[1]

[1]Laboratory for Turbulence Research in Aerospace & Combustion (LTRAC), Department of Mechanical and Aerospace Engineering, Monash University, Melbourne 3800, Australia

(Received 25 February 2021; revised 26 July 2021; accepted 17 September 2021)

In this study, large-eddy simulations are utilised to unravel the influence of the nozzle's external geometry on upstream-travelling waves in under-expanded supersonic impinging jets. Three configurations, a thin-lipped, a thin-lipped with a sponge and an infinite-lipped nozzle are considered with the other non-dimensionalised geometrical and flow variables identical for the three cases. Spectral proper orthogonal decomposition is applied to the Mack norm, i.e. the energy norm based on the stagnation energy, to obtain the spatial modes at their corresponding frequency. The spectral decomposition of the spatial modes at optimal and suboptimal frequencies is used to isolate the wavepackets into upstream- and downstream-propagating waves based on their phase velocity. It is found that the external geometry of the nozzle has a significant influence on the first-order statistics even though the governing non-dimensional parameters are the same for all three cases. Multiple peaks emerge in the energy spectra at distinct frequencies corresponding to axisymmetric azimuthal modes for each case. The downstream-propagating wavepackets have a high amplitude at the shear layer of the three jets with the mode shapes resembling Kelvin–Helmholtz instability waves, while the upstream-travelling wavepackets exist in the three regions of the near field, shear layer and inside of the jet. The barrel shock at the nozzle exit appears as a flexible shield, which prevents upstream-travelling waves from reaching the internal region of the nozzle, where the upstream-travelling waves travel obliquely with one side of the wavefront is crawling on the reflected shock while the other side is guided by the shear layer. These latter waves can reach the nozzle lip via inside of the jet. The spectral decomposition of the spatial modes at optimal and suboptimal frequencies show that all three forms of the near field, shear layer and inside jet upstream-travelling wavepackets contribute to the receptivity process while their contributions and strength are altered by the change of the external geometry of the nozzle.

**Key words:** supersonic flow, shear layer turbulence, jets

† Email address for correspondence: shahram.karami@monash.edu

© The Author(s), 2021. Published by Cambridge University Press



https://doi.org/10.1017/jfm.2021.822 Published online by Cambridge University Press

## 1. Introduction

Under-expanded supersonic jets with engineering applications range from exhausts of aircraft and rockets to mixing processes in supersonic combustion chambers, accidental leakage of pressurised fluids and cold spray additive manufacturing, and have been the subject of intense research since the theoretical study by Prandtl (1904). Flow dynamics of an under-expanded supersonic jet are more complicated than that of a subsonic jet due to the curvilinear compression shocks and high pressure and density-gradient fields (Zapryagaev, Kiselev & Gubanov 2018). Under-expanded supersonic jets are a part of the family of fluid flows classified as oscillatory flows. Some other flow configurations which are part of this family are subsonic impinging jets (Ho & Nosseir 1981; Tam & Ahuja 1990), resonance tubes, an edge-tone and a plate with a cavity (Raman & Srinivasan 2009).

In the configuration of an under-expanded supersonic impinging jet, it is recognised that the acoustic–hydrodynamic interaction is the main cause of this self-sustained oscillation (Henderson 1966; Donaldson & Snedeker 1971). Powell (1988) proposed a widely accepted conceptual theory describing the feedback oscillations based on the Rossiter mechanism found in the open cavity flow (Rossiter 1964). The main ingredients of a feedback loop are as follows: (i) shear-layer disturbances develop in the form of Kelvin–Helmholtz (K–H) instabilities; (ii) high-intensity acoustic waves are created by the interactions of K–H instabilities and the oblique shock, Mach disk and stand-off shock; (iii) high-intensity acoustic waves travel upstream; and (iv) these acoustic waves are internalised into the initial conditions of a vortical shear-layer instability at the nozzle lip via a receptivity mechanism (Karami *et al.* 2020*b*).

The early shadowgraph flow visualisation by Poldervaart & Wijnands (1974) showed that the flow structures in under-expanded supersonic free jets are significantly altered when the feedback loop is interrupted or re-enforced by a reflecting or sound-absorbing surface located in the near field of the jet. Norum (1983) studied the influence of nozzle shape on the amplitude of screech in free supersonic jet flows and found that the conditions for a given screech mode to exist are highly configuration dependent. In another experimental study by Wlezien & Kibens (1988), it was found that supersonic free jets from non-axisymmetric nozzles exhibit a wider range of acoustic properties compared with axisymmetric nozzles and that shock oscillations can be controlled or eliminated depending on the nozzle's shape. The influence of the nozzle's external geometry on the azimuthal mode selection of under-expanded supersonic impinging jets was studied using particle image velocimetry (known as PIV), acoustic measurements and ultra high-speed schlieren by Weightman *et al.* (2019) for several nozzle configurations. The authors utilised proper orthogonal decomposition (POD) to capture coherent structures, i.e. not the most energetic structures as only two components of the velocity vector were used, and observed that the thin-lip nozzle configuration contained a helical mode whereas an increase in the nozzle lip thickness resulted in a switch to an axisymmetric mode, while a secondary helical mode was also present. They concluded that altering the nozzle geometry leads to a change of the dominant instability mode.

While changing the nozzle's external geometry alters the flow field and is considered a passive control strategy, there have also been attempts to use active flow control strategies to eliminate self-sustained oscillations, for instance, by utilising plasma actuators (Gaitonde & Samimy 2011) and microjets (Alvi *et al.* 2003; Kumar, Lazic & Alvi 2009). Kumar *et al.* (2009) used microjets as an active open-loop control strategy to study the sound pressure level and the pressure force on the impingement plate, observing not only attenuation but sometimes even elimination of the discrete high-amplitude impinging tones.



https://doi.org/10.1017/jfm.2021.822 Published online by Cambridge University Press

These studies only focused on the influence of the nozzle and near obstacle geometries, i.e. a passive control, on the global dynamics of the flow or the manipulation of the near field instabilities utilising plasma actuators or microjets, i.e. an active control, while the upstream waves and their contribution to the receptivity process, which is the main contributor to the altered dynamics caused by the geometrical change, has received little attention. To the best of our knowledge, the influence of the external geometry of the nozzle on the upstream-travelling waves and receptivity process in the configuration of under-expanded supersonic impinging jets has not been investigated. Hence, motivated by recent experimental observations of the influence of the external geometry of the nozzle on the global hydrodynamic and acoustic physics of under-expanded supersonic impinging jets (Weightman *et al.* 2019) and our previous study of receptivity in this flow (Karami *et al.* 2020*b*), the primary objective of this study is to investigate the nature of upstream-travelling waves and their contributions to the receptivity process as a function of the external geometry of the nozzle. For this purpose, spectral proper orthogonal decomposition (SPOD) is utilised to obtain the single frequency energy ranked coherent structures, i.e. a mode shape with a well-described and unique frequency, where the total energy, known as the Mack energy norm (Mack 1984; Hanifi, Schmid & Henningson 1996; Freund & Colonius 2002; Tumin & Reshotko 2003; Ray, Cheung & Lele 2009; Paredes *et al.* 2016), is used as the energy norm. It is noted that obtaining the energy norm based on the Mack energy is not feasible in experimental studies of this flow configuration due to difficulty in simultaneous measurements of the three components of the velocity and pressure fields.

In recent years, there have been considerable developments in data-driven techniques to reveal the characteristics of coherent structures in turbulent flows (Bagheri *et al.* 2009; Schmid 2010; Sieber, Paschereit & Oberleithner 2016; Le Clainche & Vega 2017; Le Clainche, Vega & Soria 2017; Towne, Schmidt & Colonius 2017). Spectral proper orthogonal decomposition as a data-driven technique was first introduced by Lumley (1970). This original POD method identifies energy-ranked modes where each oscillates at a single frequency, and has been largely overlooked since its inception despite its advantages over the common spatial form of POD (Sirovich 1987*a*), i.e. the snapshot method (Kostas, Soria & Chong 2005). Glauser, Leib & George (1987) applied the SPOD method to experimental hot wire measurements of the velocity in the shear layer of an axisymmetric jet to study the coherent structures in an axisymmetric jet showing that nearly all the energy of the flow was accumulated in the first three modes. In another study, Delville *et al.* (1999) used SPOD to study the coherent structures in a plane turbulent mixing layer where the first mode was found to be dominant containing nearly 50 % of the turbulent kinetic energy. Stahl, Prasad & Gaitonde (2021) performed large eddy simulation (LES) of single and dual impinging jets and applied the SPOD method to pressure fluctuation fields to investigate the changes in the jet dynamics when another jet is added alongside to form a dual impinging jet arrangement. There are a number of techniques in the literature to compute SPOD modes (Citriniti & George 2000; Gordeyev & Thomas 2000; Towne *et al.* 2017). In this study, we used the procedure developed by Towne *et al.* (2017), which has been comprehensively reviewed in Schmidt & Colonius (2020), as it is found to be computationally more efficient compared with others. Spectral proper orthogonal decomposition utilises the Fourier transform to decompose the dynamics into the frequency domain and then applies the energy ranked optimisation at each discrete frequency to find the mode shape associated with that frequency. Hence, it is used in this study as a more rigorous approach to investigate upstream-travelling waves in the configuration of under-expanded supersonic impinging jets.



https://doi.org/10.1017/jfm.2021.822 Published online by Cambridge University Press

The rest of the manuscript is organised as follows. In § 2, the numerical method and configurations of this study are presented. A brief discussion of SPOD follows in § 3, for completeness. The results, including mean flow fields, SPOD spectra and mode shapes at dominant frequencies and upstream and downstream wavepackets at these discrete frequencies are presented in § 4 with discussion and concluding remarks in § 5.

## 2. Configurations and numerical methods

The configuration is an under-expanded supersonic impinging jet with the nozzle-to-wall distance of $h = 2d$, where $d$ is the jet diameter. In this study, three external nozzles with a thin-lipped nozzle, a thin-lipped nozzle with a sponge, and an infinite-lipped nozzle are considered. The schematics of the $x$–$r$ plan view at $\theta = 0$ of these three configurations are presented in figure 1.

An in-house developed high-fidelity LES parallel multiblock code (ECNSS) (Karami *et al.* 2019) is used to solve the filtered compressible conservation equations of mass, momentum and total energy in cylindrical coordinates. This code has been validated extensively in previous studies (Stegeman *et al.* 2016*a*; Stegeman, Soria & Ooi 2016*b*; Karami, Edgington-Mitchell & Soria 2018*a*; Karami *et al.* 2018*b*, 2019, 2020*b*; Amjad *et al.* 2020). The subgrid-scale terms are computed using Germano's dynamic model with the adjustment proposed by Lilly (1992). A sixth-order central finite difference method is applied in the smooth regions in all spatial directions, while a fifth-order weighted essentially non-oscillating scheme (known as WENO) with local Lax–Friedrichs flux splitting is used in the discontinuous regions. A novel shock identification and capturing method is used to capture the discontinuous regions (Karami *et al.* 2019). The temporal integration is performed using a fourth-order, five-step Runge–Kutta scheme (Kennedy & Carpenter 1994; Kennedy, Carpenter & Lewis 2000). The centreline numerical singularity in cylindrical coordinates is treated with the procedure developed by Mohseni & Colonius (2000) as an accurate method that is simple to implement (Fukagata & Kasagi 2002; Morinishi, Vasilyev & Ogi 2004; Livermore, Jones & Worland 2007; Bogey, Marsden & Bailly 2011; Gojon & Bogey 2017). The modified Navier–Stokes equations are considered in our implementation of the wall boundary condition where all the convective terms vanish in the case of a no-slip/no-penetration wall boundary condition. For the sixth-order spatial discretisation applied here, four extra cell points are used as ghost cells where the primitive variables are evaluated using the Taylor extrapolation for these points considering the no-slip, adiabatic wall condition. The approach of treating the wall boundary condition by introducing ghost cells has been proved to be stable and effective (Tam & Dong 1994; Colonius & Lele 2004). This approach also allows the internalisation of the acoustic waves into a shear-layer instability through a receptivity mechanism at the nozzle lip (Karami *et al.* 2020*b*). The interested reader is referred to Karami *et al.* (2019) for further details on the numerical method, the novel shock identification and capturing method and the LES code. The mean inlet axial velocity is specified using the hyperbolic-tangent function suggested by (Bodony & Lele 2005) with an inlet momentum thickness of $0.04d$ (Bogey *et al.* 2011; Karami *et al.* 2020*b*) and a laminar inlet flow. The assumption of laminar inlet flow is considered to be valid as the nozzle of the under-expanded supersonic jet has a high contraction ratio similar to previous experimental studies (Edgington-Mitchell, Honnery & Soria 2014; Amili *et al.* 2015*a*,*b*; Soria & Amili 2015); hence, the inlet turbulence is considered to be negligible. The Reynolds number based on inlet velocity and jet diameter is 50 000, which is similar to our previous studies (Karami *et al.* 2018*a*, 2020*a*,*b*; Sikroria *et al.* 2020), to maintain the LES resolution requirement under acceptable computational cost (Kawai & Lele 2010).



https://doi.org/10.1017/jfm.2021.822 Published online by Cambridge University Press

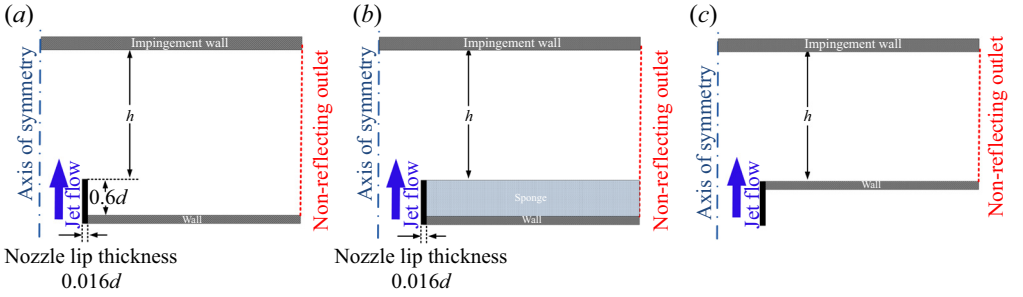



Figure 1. Schematic of the three configurations with the thin-lipped nozzle lip with reflecting surface (*a*), the thin-lipped nozzle lip with the sponge region to tapper reflected acoustic waves (*b*) and the infinite-lipped nozzle (*c*) (it is noted that the configuration is axisymmetric, hence only the $x$–$r$ plan view at $\theta = 0$ is shown).

| Region | $L_x \times L_r \times L_\theta$ | $N_x \times N_r \times N_\theta$ | $(\Delta x_{min}, \Delta x_{max})$ | $(\Delta r_{min}, \Delta r_{max})$ |
|---|---|---|---|---|
| 1 | $0.03 \times 0.5 \times 2\pi$ | $16 \times 48 \times 96$ | $(1.9\times10^{-3}, 2.1\times10^{-3})$ | $(0.9\times10^{-3}, 2.5\times10^{-3})$ |
| 2 | $2.0 \times 0.5 \times 2\pi$ | $480 \times 48 \times 96$ | $(1\times10^{-3}, 6\times10^{-3})$ | $(0.9\times10^{-3}, 2.5\times10^{-3})$ |
| 3 | $2.0 \times 0.016 \times 2\pi$ | $480 \times 16 \times 96$ | $(1\times10^{-3}, 6\times10^{-3})$ | $(0.96\times10^{-3}, 1.2\times10^{-3})$ |
| 4 | $2.0 \times 11.48 \times 2\pi$ | $480 \times 368 \times 96$ | $(1\times10^{-3}, 6\times10^{-3})$ | $(1.25\times10^{-3}, 15\times10^{-2})$ |
| 5 | $0.6 \times 11.48 \times 2\pi$ | $192 \times 368 \times 96$ | $(2\times10^{-3}, 7\times10^{-3})$ | $(1.2\times10^{-3}, 15\times10^{-2})$ |

Table 1. Lengths and grid points for each block in the computational domain as depicted in figure 2. All dimensions are normalised with the nozzle diameter $d$.

The nozzle pressure ratios (NPR) (i.e. the ratio between the stagnation pressure measured in the jet plenum and the ambient pressure) is 3.4. This NPR is higher than the critical NPR (= 1.893 for dry air); hence, the nozzle is choked and the nozzle exit Mach number is unity for all three cases. The size of the computational domain in the radial direction is $12d$. The details of the computational grid are provided in table 1. A uniform grid is employed in the azimuthal direction, $\theta$. In the axial direction, $x$, a fine grid is used near the nozzle and near the impingement wall. In the radial direction, $r$, a fine grid is used in the mixing layer region with a polynomial stretching of the grid points towards the jet's centre and the far field. Similar to our previous study (Karami *et al.* 2020*b*), the maximum mesh spacing of $0.04d$ for $r < 8.5d$ is used which allows the capture of the propagation of acoustic waves with Strouhal numbers up to 5.0. This resolution leads to over $27 \times 10^6$ grid points for the thin-lipped nozzle with reflecting surface case and the thin-lipped nozzle with the sponge region case and over $20 \times 10^6$ grid points for the infinite-lipped nozzle case. Davidson (2009) recommends a minimum of eight computational grid points to represent the largest structures for a coarse LES, while a recent study by Pelmard, Norris & Friedrich (2018) suggests that more than 16 computational grid points are required to represent the largest structures in a well-resolved LES. Based on these recommendations, 16 computational grid points are used in the shear line region, i.e. region 3 in figure 2.

The simulations are run for 204.8 acoustic time units ($ta_o/d$, where $t$ is time and $a_o$ is the speed of sound) after the transient period. The transient period to wash out the initial conditions is approximately 50 acoustic time units. The three-dimensional flow fields after the transient period are stored every 0.05 acoustic time units, which yields 4096 three-dimensional snapshots. It should be noted that the equations and all other



https://doi.org/10.1017/jfm.2021.822 Published online by Cambridge University Press

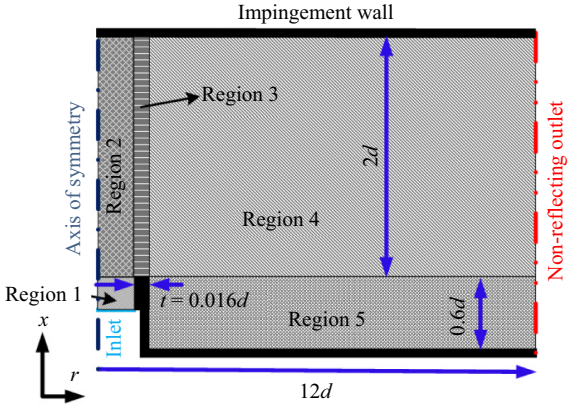



Figure 2. Schematic of the domain of the simulation with different regions highlighted (it is noted that the configuration is axisymmetric, hence only the $x$–$r$ plan view at $\theta = 0$ is shown).

parameters are non-dimensionalised with respect to the nozzle diameter ($d$), speed of sound ($a_o$) and viscosity at atmospheric temperature (the non-dimensionalised variables are used throughout this paper). The sound absorption sponge is modelled as a sponge region where an unphysical term of form $\sigma(q_{ref} - q)$ ($q$ is a primitive variable and $q_{ref}$ is the reference primitive variable) is added to the right-hand side of the Navier–Stokes equations to force the flow to an atmospheric reference temperature and pressure which reduces the reflection of acoustic waves from the reflective wall attached to the root of the nozzle. The parameter $\sigma$ is an inverse time scale representing the strength of the sponge region (Almgren *et al.* 2008). It has a constant value in the sponge region and zeros outside of the sponge region where the transition from zero to $\sigma$ occurs through a quadratic spatial function (Colonius, Lele & Moin 1997; Bodony 2006; Haghiri *et al.* 2018). Based on our numerical experiments and previous studies (Brès *et al.* 2018; Haghiri *et al.* 2018; Bodony 2006; Colonius *et al.* 1997), a value of $\sigma = 0.3$ is used in this study.

## 3. The mathematical background of SPOD

The space-only POD (Lumley 1967, 1981; Sirovich 1987*a*,*b*,*c*) assumes the flow variables are separable into time and space. Based on this assumption, flow variables are separated into spatial mode shapes, i.e. base functions that are ranked based on their energy content, and mode coefficients, i.e. mode dynamics which may have a broad spectral characteristic. The SPOD (Tutkun, Johansson & George 2008; Hellström & Smits 2014; Tutkun & George 2017; Schmidt *et al.* 2018; Towne, Schmidt & Colonius 2018; Karami & Soria 2018; Milani *et al.* 2020), however, uses the Fourier transform in time to decompose the dynamics in the frequency domain and then applies the energy ranked optimisation at each discrete frequency to find the mode shape associated with that frequency. The Fourier transformation guarantees that the mode shape has a well-described frequency. A brief description of the SPOD approach is presented here for completeness, while the interested reader can refer to a recent paper on the application of the SPOD method and its properties by Schmidt & Colonius (2020). The kernels of both space-only POD and SPOD are an energy norm. It is known that the jet flow is homogeneous in the azimuthal direction and considering that the under-expanded supersonic impinging jets of this study is statistically



https://doi.org/10.1017/jfm.2021.822 Published online by Cambridge University Press

stationary, fluctuations of every flow variable of $q$ can be expressed as

$$q'(x, r, \theta, t) = q(x, r, \theta, t) - \bar{q}(x, r), = \sum_{-N_\theta/2}^{N_\theta/2} q_m(x, r, t) \exp \mathrm{i}m\theta, \tag{3.1}$$

where $\bar{q}$ is the temporally azimuthally averaged field, $N_\theta$ is the number of computational grid points in the azimuthal direction and $m$ is azimuthal mode number. Using the common Euclidean inner product, an energy norm is defined as

$$\begin{aligned}&\iint_D \langle q_m^* W q_m \rangle \,\mathrm{d}x\,\mathrm{d}r \\ &\quad = \iint_D [\alpha_1 (u_x^*)_m (u_x)_m + \alpha_2 (u_r^*)_m (u_r)_m + \alpha_3 (u_\theta^*)_m (u_\theta)_m + \alpha_4 a_m^* a_m + \alpha_5 p_m^* p_m] \,\mathrm{d}x\,\mathrm{d}r,\end{aligned} \tag{3.2}$$

where $*$ denotes the complex conjugate, $(u_x, u_r, u_\theta)$ are the three components of the velocity vector, $a$ is the local speed of sound, $p$ is the pressure and the vector $\boldsymbol{\alpha} = [\alpha_1, \alpha_2, \alpha_3, \alpha_4, \alpha_5]$ determines the specific norm. Choosing $\boldsymbol{\alpha} = [1, 1, 1, 2/(\gamma - 1), 0]$ recovers the stagnation enthalpy norm used by Rowley (2002) for compressible flows and is also used in this study as it is found to be more relevant than the turbulent kinetic energy norm (i.e. $\boldsymbol{\alpha} = [1, 1, 1, 0, 0]$), which is often used in incompressible flows. In this context, the norm that is commonly used in experimental studies can be obtain by $\boldsymbol{\alpha} = [1, 1, 0, 0, 0]$ which approximates the turbulent kinetic energy using two components of the velocity vector.

Assume that the flow variables of interest, based on the definition of the energy norm, are available for $N$ time instants which are decomposed in the homogeneous direction (i.e. the azimuthal direction in this study) and equally spaced in time, then the dataset can be organised in a compact matrix form as

$$\boldsymbol{Q}_m = [\boldsymbol{q}_{1,m}, \boldsymbol{q}_{2,m}, \ldots, \boldsymbol{q}_{N,m}], \tag{3.3}$$

where $m$ is the azimuthal mode number. The matrix $\boldsymbol{Q}_m$ has a dimension of $M \times N$ where $M$ is the number of spatial points (the radial grid points times the axial grid points) times the number of variables. The converged estimation of the cross-spectral density tensor can be obtained by averaging the spectra over multiple realisations of the flow (Bendat & Piersol 1966). Firstly, the dataset is partitioned into smaller blocks or segments ($N_b$) with an overlap of $N_{ovlp}$, each of which represents an ensemble realisation of the flow. A temporal discrete Fourier transform of each block is then calculated, $\hat{\boldsymbol{Q}}_m^{(b)}$. A Hanning window is used to reduce the discontinuities with a hypothetical next period and spectral leakage. A new data matrix is formed at the $k$th frequency by collecting all of the Fourier realisations of the blocks $\hat{\boldsymbol{Q}}_{(m,f_k)}$. This yields the estimated cross-spectral density tensor at frequency $f_k$ as

$$\hat{\boldsymbol{S}}_{(m,f_k)} = \hat{\boldsymbol{Q}}_{(m,f_k)} \hat{\boldsymbol{Q}}^*{}_{(m,f_k)}. \tag{3.4}$$

For a given frequency, the SPOD modes are found as the eigenvectors $\boldsymbol{\Psi}_{\boldsymbol{m},\boldsymbol{f_k}} = [\psi_{m,f_k}^{(1)} \psi_{m,f_k}^{(2)} \cdots \psi_{m,f_k}^{(n_b)}]$, and the total energy as the corresponding eigenvalues $\boldsymbol{\Lambda}_{\boldsymbol{m},\boldsymbol{f_k}} = diag(\lambda_{m,f_1}^{(1)} \lambda_{m,f_2}^{(2)} \cdots \lambda_{m,f_{n_f}}^{(n_b)})$ of the weighted cross-spectral density matrix $\hat{\boldsymbol{S}}_{(m,f_k)}$ which is



https://doi.org/10.1017/jfm.2021.822 Published online by Cambridge University Press

defined as

$$\hat{\boldsymbol{S}}_{(m,fk)}\boldsymbol{W}\boldsymbol{\Psi}_{\boldsymbol{m},\boldsymbol{fk}} = \boldsymbol{\Psi}_{\boldsymbol{m},\boldsymbol{fk}}\boldsymbol{\Lambda}_{\boldsymbol{m},\boldsymbol{fk}}. \tag{3.5}$$

The eigenvalues are ordered from the largest to the smallest. The eigenvector corresponding to the largest eigenvalue is the leading or optimal mode, and the subsequent smaller eigenvalues (i.e. lower-energy modes) are suboptimal modes at each azimuthal mode number.

## 4. Results

### 4.1. *Influence of the external geometry of the nozzle on the mean flow field*

The influence of the nozzle's external geometry has been studied experimentally (Poldervaart & Wijnands 1974; Weightman *et al.* 2017), however, numerical studies in this spectrum are scarce. Microphone measurements are commonly utilised to analyse the acoustic near field of free and impinging supersonic jets (Semlitsch *et al.* 2020; Edgington-Mitchell *et al.* 2014). Some of these studies show that the supersonic jet flows are very sensitive to the experimental set-up. Therefore, first-order statistics are presented in this section as it is found that changes in the nozzle's external geometry modify them significantly.

Figure 3 shows contour plots of the ensemble-averaged streamwise velocity (*a–c*), radial velocity (*d–f*), as well as the pressure (*g–i*) for the thin-lipped nozzle (*a*,*d*,*g*), thin-lipped nozzle with the sponge (*b*,*e*,*h*) and infinite-lipped nozzle (*g*,*h*,*i*). Starting with the ensemble-averaged streamwise velocity, the streamlines near the nozzle lip with a zoomed-in view in the black rectangle marked as 'A' show that changes in the external geometry of the nozzle have a significant effect on entrainment in the region near the nozzle lip. It is noted that the sponge region alters the pressure field; hence, it alters the acoustic feedback loop, which leads to the inevitable alteration of the mean flow field. Compared with the thin-lipped nozzle, the Mach disk location, marked as 'B', moves slightly upstream in the case of the thin-lipped nozzle with the sponge, while it moves downstream in the configuration of the infinite-lipped nozzle.

Another physically interesting phenomenon is the formation of a recirculation zone at the impingement region created by the large pressure drop behind the strong shock and the condition required for its formation is still a topic of debate (Dauptain, Gicquel & Moreau 2012). The streamlines at this region are shown for all three cases in the zoomed-in view in the black rectangle marked as 'C' in figure 3(*a–c*). The recirculation bubble present in the case of the thin-lipped nozzle, it nearly disappears in the case of the thin-lipped nozzle with the sponge, and reappears again in the case of the infinite-lipped nozzle. Previous studies (Dauptain, Cuenot & Gicquel 2010; Dauptain *et al.* 2012) found that the formation of a recirculation bubble depends on the NPR, nozzle-to-wall distance and impingement plate dimension while the results of this study clearly for the first time show the process is more complex and the external geometry of nozzle is another important parameter that must be taken into account.

The ensemble-averaged radial velocities for the three cases are shown in figure 3(*d–f*) where the alteration to the Mach disk and the triple point is easily identified. These alterations are also clearly noticeable in the animations of the density gradient, which are provided as supplementary material available at https://doi.org/10.1017/jfm.2021.822. The recirculation zone where the radial velocity is negative is also clearly observable in these contour plots. One clear difference between the three cases of this study is that flow separation in the wall jet region which is present for the thin-lipped nozzle and faded as the thin-lipped nozzle is modified by adding the sponge (serving as a sound absorber) and



https://doi.org/10.1017/jfm.2021.822 Published online by Cambridge University Press

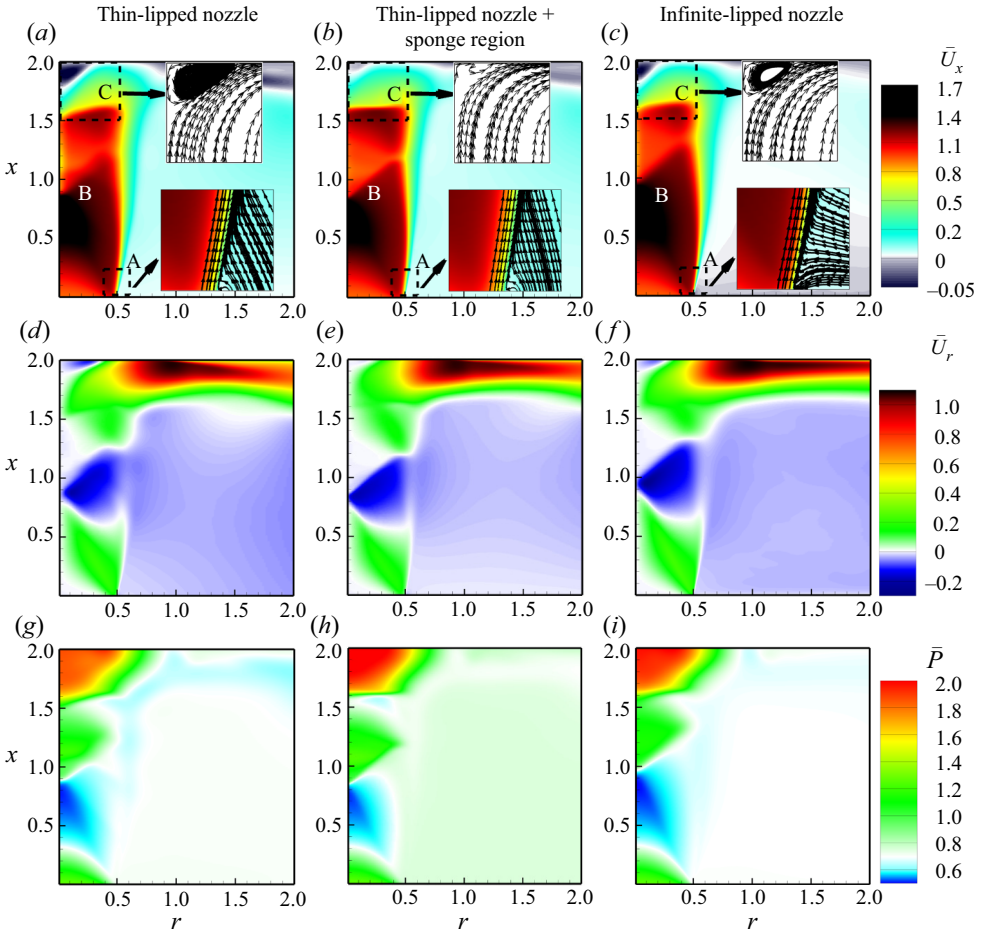



Figure 3. Contour plots of ensemble-averaged streamwise velocity (*a–c*), radial velocity (*d–f*) and pressure (*g–i*) for the thin-lipped nozzle (*a*,*d*,*g*), thin-lipped nozzle with the sponge (*b*,*e*,*h*) and infinite-lipped nozzle (*c*,*f*,*i*).

the solid wall. This flow separation is clear in the wall jet region in figure 3(*d–f*) where the ensemble-averaged streamwise velocity is negative and the radial velocity near to the impingement wall is low. Ensemble-averaged pressure fields of the three cases of this study are presented in figure 3(*g–i*) where the mean pressure increases at the impingement wall as the nozzle lip is changed to the infinite-lipped nozzle. The stand-off shock is found to be stronger in the case of a thin-lipped nozzle with the sponge.

### 4.2. *Coherent structures obtained from SPOD*

The kernel of SPOD is a fast Fourier transform (known as FFT) of multiple flow realisations. The simulations have 4096 three-dimensional snapshots that are equally spaced in time, with a time step of 0.05 acoustic time units. A window size of 1024 snapshots with 75 % overlap produces 13 blocks that are used to obtain the SPOD modes. The SPOD was also evaluated using a window size of 512 snapshots with 75 % overlap, as well as other combinations of the window size and overlap, to investigate the sensitivity of the results to window size and overlap. These alternate combinations did not



https://doi.org/10.1017/jfm.2021.822 Published online by Cambridge University Press

significantly change the results: changes in the leading eigenvalues did not exceed 0.1 % in both the optimal and the suboptimal frequencies.

Figure 4 presents the first three SPOD modes ($i = 1$, 2 and 3) of the first three azimuthal mode numbers of $m = 0$, 1 and 2 for the thin-lipped nozzle (*a*), the thin-lipped nozzle with the sponge (*b*) and infinite-lipped nozzle (*c*). All three cases show that the axisymmetric mode, $m = 0$, is dominant, with multiple peaks observed in the spectra. There is a low Strouhal number peak in all three cases (marked with a red circle and arrow) that is associated with the bouncing of the acoustic waves between the impingement wall and the wall attached to the nozzle. As shown later, these low-frequency modes have high amplitude spatial components in the wall jet region with a slow phase velocity. The low-frequency peaks are followed by three peaks and their harmonics in all three cases, which are shown by black filled, black open and black cyan-filled circles. The optimal frequency, also called the 'leading mode', is marked with a black open circle and a blue arrow. The optimal frequency is an order of magnitude stronger in both cases that used the thin-lipped nozzle. In contrast, the optimal and suboptimal frequencies have comparable amplitudes in the case of the infinite-lipped nozzle, which is more apparent in the harmonics of this case. The distribution of energy in the frequency domain of the case with an infinite-lipped nozzle leads to an early conclusion that the infinite-lipped nozzle in this set-up suppresses the presence of a strong and dominant peak in spectra, which is commonly interpreted as a screech. In all three cases of this study, a large gap is observed between the first and second SPOD eigenvalues, indicating a low-rank behaviour. The low-rank behaviour is also reported in subsonic free jet flows (Towne *et al.* 2017). However, as shown in figure 4, this low-rank behaviour is comprehensible at optimal and suboptimal frequencies in the under-expanded supersonic jet configuration in this study, as the gap is an order of magnitude larger.

The spatial distributions of the first SPOD modes of the first azimuthal wavenumber of the streamwise velocity ($\psi_{i=0}^{m=0} : u_x$) and the local speed of sound ($\psi_{i=0}^{m=0} : a$) at optimal and suboptimal frequencies are presented in figure 5 for the thin-lipped nozzle case. As mentioned, the peaks at low frequencies have high amplitude wavepackets in the wall jet region. In the thin-lipped nozzle configuration, there are two low Strouhal numbers of $St_j = 0.18$ and 0.36 that have such a spatial pattern. The lower Strouhal number (i.e. $St_j = 0.18$) has the strongest wavepackets while the higher Strouhal number (i.e. $St_j = 0.36$) appears as the harmonic of the first Strouhal number with approximately the same amplitude but a different wavelength (see figure 5*a–d*). The velocity component ($\psi_0^0 : u_x$) is stronger than the local speed of sound component ($\psi_0^0 : a$), indicating that these two modes are hydrodynamically driven coherent structures in the wall jet, and oscillations at these low frequencies are dictated by the bouncing of acoustic waves between the impingement wall and the wall attached to the root of the nozzle. The spatial pattern of the SPOD mode at $St_j = 0.58$ is more intense in the shear layer in both velocity and local speed of sound components, with a wavepacket emanating from an acoustic source located near the impingement wall (approximately at $r = 1.8$) alternating with a weakly positive/negative sign at an angle of 45°. The spatial pattern of the SPOD mode at $St_j = 0.72$, which is the optimal mode of this case, develops a continuous wavepacket in the shear layer of the jet and is convected in the wall jet as shown in both the velocity and local speed of sound components. The spatial wavelength of this wavepacket before fading away in the wall jet does not vary in the spatial domain, indicating a constant phase velocity. There are also wavepackets in the near field and outside the jet's periphery, that are acoustic in nature, i.e. the vorticity is negligible outside the shear layer. These wavepackets appear as a cellular pattern because of the reflection of the acoustic waves



https://doi.org/10.1017/jfm.2021.822 Published online by Cambridge University Press

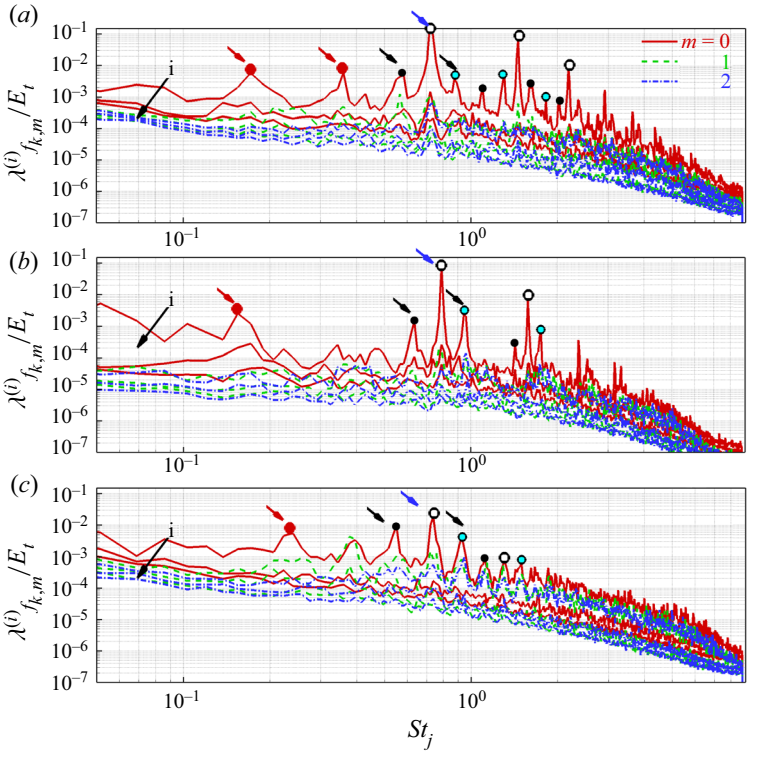



Figure 4. The SPOD eigenvalue spectra of the first three azimuthal mode numbers normalised by cumulative energy of these azimuthal modes for the thin-lipped nozzle (*a*), thin-lipped nozzle with the sponge (*b*) and infinite-lipped nozzle (*c*).

from the wall attached to the nozzle's root. The spatial contour map of the SPOD mode at $St_j = 0.88$, presented in figures 5(*i*) and 5(*j*), has a similar mode shape to that at $St_j = 0.72$, with a different wavelength.

The results for the thin-lipped nozzle with the sponge, presented in figure 6, show the spatial pattern of the first SPOD modes of the first azimuthal wavenumber of the streamwise velocity ($\psi_0^0 : u_x$) and the local speed of sound ($\psi_0^0 : a$) at the optimal and suboptimal frequencies. At the lowest suboptimal Strouhal number ($St_j = 0.15$ which is approximately 15 % lower than the lowest suboptimal Strouhal number of the thin-lipped nozzle case), an intense wavepacket appears in the wall jet region, which is more evident in the velocity component than the local speed of sound component. However, its strength is weaker than the coherent structures in the shear layer of the optimal mode presented in figure 6(*e*). It should be noted that the behaviour is different in the thin-lipped nozzle case and the strength of the low-frequency coherent structures in the wall jet is comparable to the coherent structures in the shear layer of the optimal mode (see figures 5*a* and 5*g*). The spatial mode shape of the suboptimal mode (i.e. at $St_j = 0.63$ which is approximately 9 % higher than the suboptimal mode of the thin-lipped nozzle case) is presented in figures 6(*c*) and 6(*d*). The spatial distribution of this mode shows that a weak wavepacket is travelling in the shear layer and is diverted into the wall jet and fades away in the wall jet region. Similar to the thin-lipped nozzle case, the mode shape of the optimal mode (i.e. at $St_j = 0.79$, which is approximately 9.5 % higher than that of the thin-lipped nozzle case) shows that a coherent, K–H-like wavepacket develops in the shear layer and travels in



https://doi.org/10.1017/jfm.2021.822 Published online by Cambridge University Press

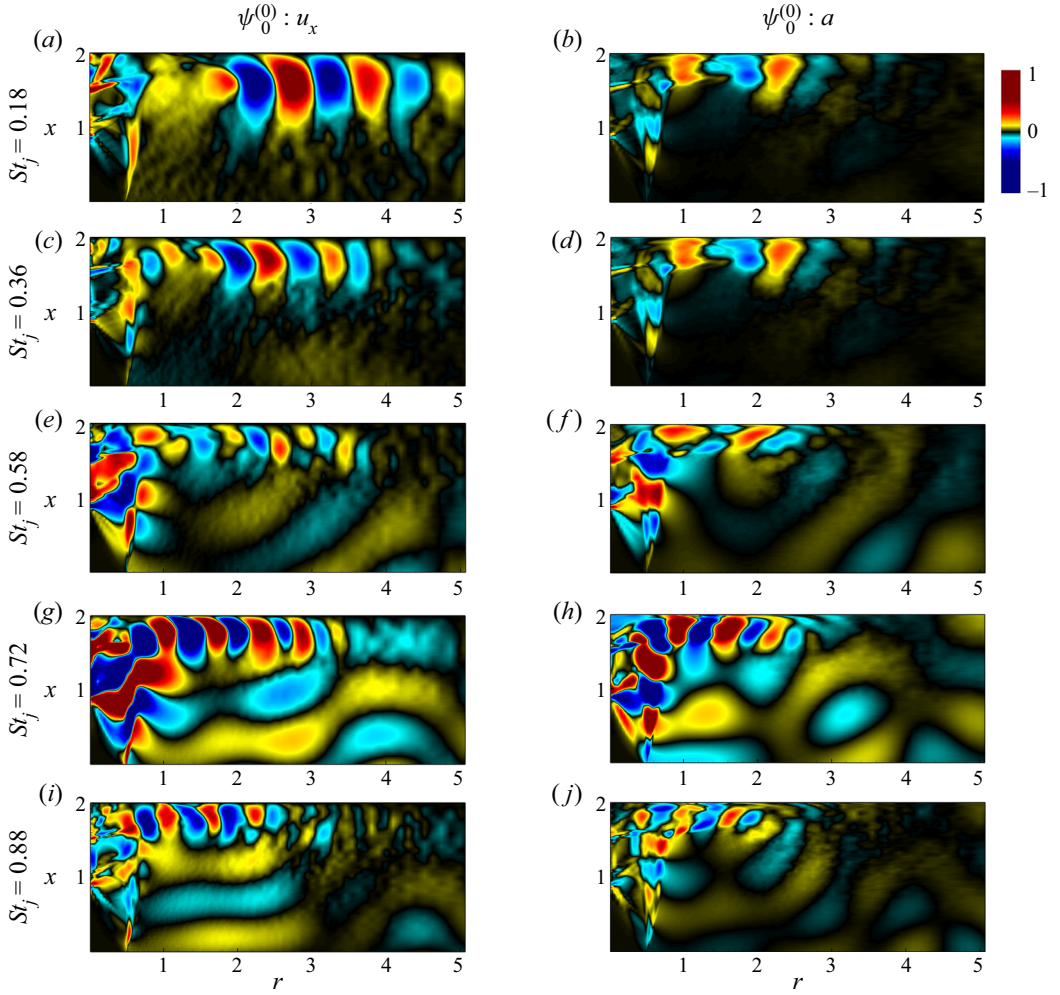



Figure 5. Four dominant SPOD modes of the streamwise velocity (*a*,*c*,*e*,*g*) and the local speed of sound (*b*,*d*,*f*,*h*) for the first azimuthal wavenumber ($m = 0$) for the thin-lipped nozzle.

the wall jet region. One important difference compared with the thin-lipped nozzle case is the significantly weaker cellular pattern of the near field acoustic field, which is due to the damping of acoustic waves by the sponge region in this configuration. The high Strouhal number suboptimal mode ($St_j = 0.94$) has a similar mode shape to the optimal mode but with a different and shorter wavelength, as expected.

The results show that reducing the strength of the acoustic wave by using the sponge region attached to the thin-lipped nozzle, which serves as an imperfect sound absorber, has a significant effect on the SPOD modes, with a shift of approximately 10 % in the optimal and suboptimal Strouhal numbers. However, the sponge region used in this study could not eliminate the peaks in the spectra as achieved by Weightman *et al.* (2019) using foam. It is worth noting that obtaining such a perfect sound absorbing surface numerically is a challenging task and requires multiple high-fidelity simulations.

After determining the influence of the imperfect sound absorber (i.e. the sponge region attached to the thin-lipped nozzle), the next step is to investigate how the modes change



https://doi.org/10.1017/jfm.2021.822 Published online by Cambridge University Press

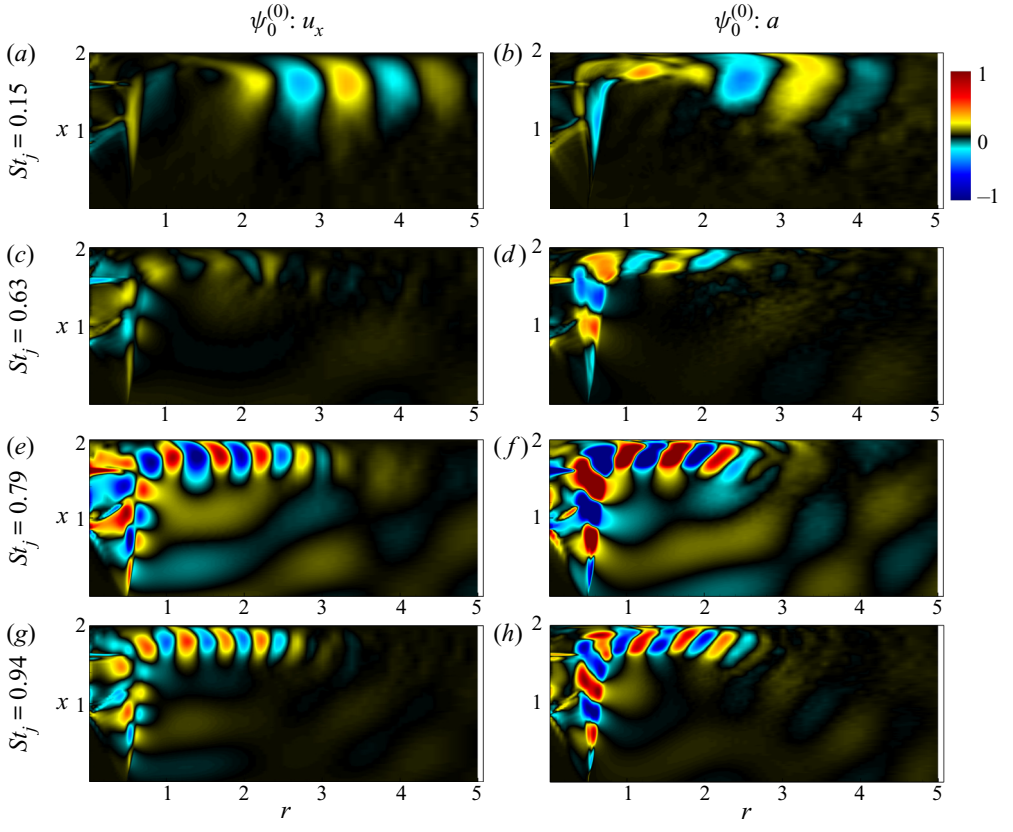



Figure 6. Four dominant SPOD modes of the streamwise velocity (*a*,*c*,*e*,*g*) and the local speed of sound (*b*,*d*,*f*,*h*) for the first azimuthal wavenumber ($m = 0$) for the thin-lipped nozzle with the sponge.

when the acoustic absorber (the sponge) is replaced with a perfectly reflecting surface, for example, a wall attached to the thin-lipped nozzle (the 'infinite-lipped nozzle'). Figure 7 shows the first SPOD modes of the first azimuthal wavenumber of the streamwise velocity ($\psi_0^0 : u_x$) and the local speed of sound ($\psi_0^0 : a$) at optimal and suboptimal frequencies. At the low Strouhal number of $St_j = 0.24$, approximately 30 % higher than the thin-lipped nozzle, the wavepackets are intense at the Mach disk location, stand-off shock and oblique shock. Like the other two cases, a coherent wavepacket appears in the wall jet region at this low Strouhal number. The optimal mode (i.e. $St_j = 0.74$) and suboptimal modes (i.e. $St_j = 0.55$ and 0.92) show a similar trend of the development of the wavepackets in the shear layer, diversion of these wavepackets into the wall jet region and weakening as they travel in the wall jet region. The near field local speed of sound components of these modes show cellular patterns with wavelengths that shorten as the Strouhal number increases. In light of these observations, the perfectly reflecting surface seems to shift the optimal and suboptimal Strouhal numbers and suppress the optimal mode. This observation is consistent with the experimental microphone measurement of Weightman *et al.* (2019), where they studied the same NPR as this study but with a different nozzle-to-wall distance. They found that the dominant Strouhal number of the infinite-lipped nozzle case shifted and its amplitude weakened compared with the finite-lipped nozzle cases.



https://doi.org/10.1017/jfm.2021.822 Published online by Cambridge University Press

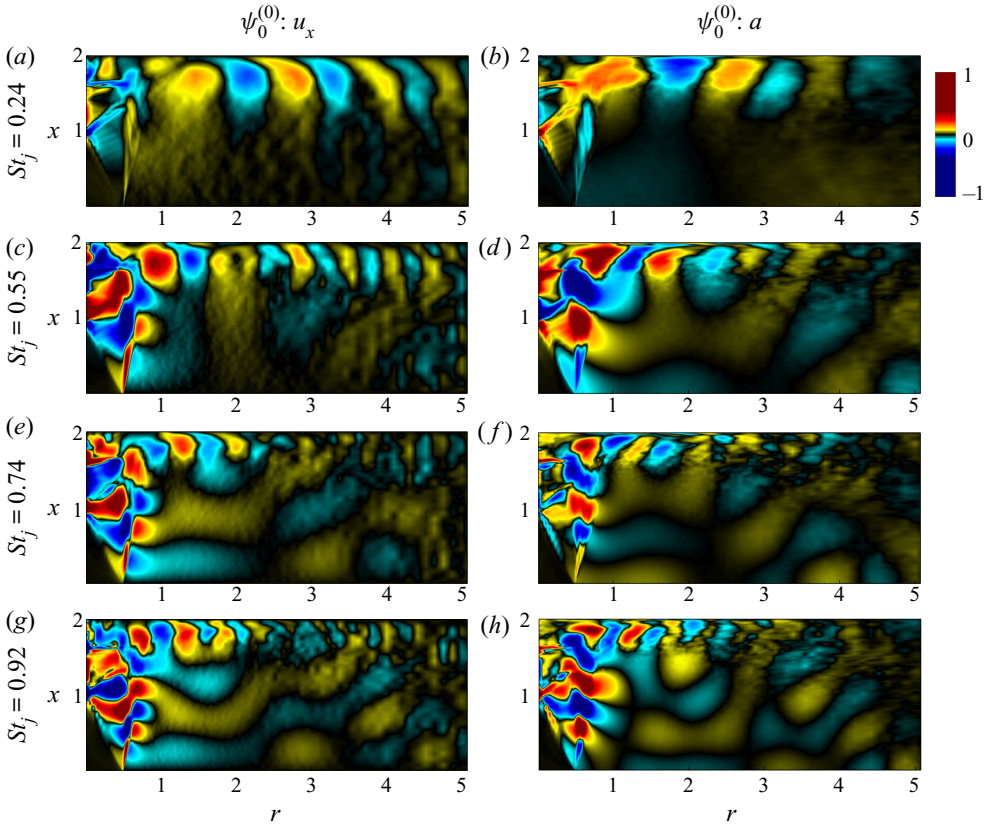



Figure 7. Four dominant SPOD mode of the streamwise velocity (*a*,*c*,*e*,*g*) and the local speed of sound (*b*,*d*,*f*,*h*) for the first azimuthal wavenumber ($m = 0$) for the infinite-lipped nozzle.

### 4.3. *Upstream-propagating and downstream-propagating waves of the dominant coherent features*

The spectra presented in figure 4 and mode shapes presented in figures 5, 6 and 7 show that changing the external geometry of the nozzle while keeping all other non-dimensional parameters identical significantly alters both the spectra and the mode shapes (i.e. the optimal and suboptimal wavepackets). These findings are consistent with the previous experimental studies of Weightman *et al.* (2019). However, in light of the time-resolved, three-dimensional fields of all primitive variables that contribute to the energy norm available from the LES, this phenomenon was analysed comprehensively and with a great level of detail for the first time in under-expanded supersonic impinging jets.

A little addressed yet physically relevant phenomenon in under-expanded supersonic flows is upstream-travelling waves (Edgington-Mitchell *et al.* 2018, 2021) and their contributions to closing the feedback loop (Powell 1953). Edgington-Mitchell *et al.* (2018) applied POD to two-component–two-dimensional (2C–2D) velocity measurements of a moderately under-expanded supersonic free jet. They used the first pair of POD modes and the screech frequency obtained using a microphone measurement to construct the time evolution of the dominant wavepacket, and a spatial decomposition of these modes to separate the upstream and downstream waves at the screech frequency. This approach may not be valid in the configuration of this study, as the spectra obtained using the SPOD



https://doi.org/10.1017/jfm.2021.822 Published online by Cambridge University Press

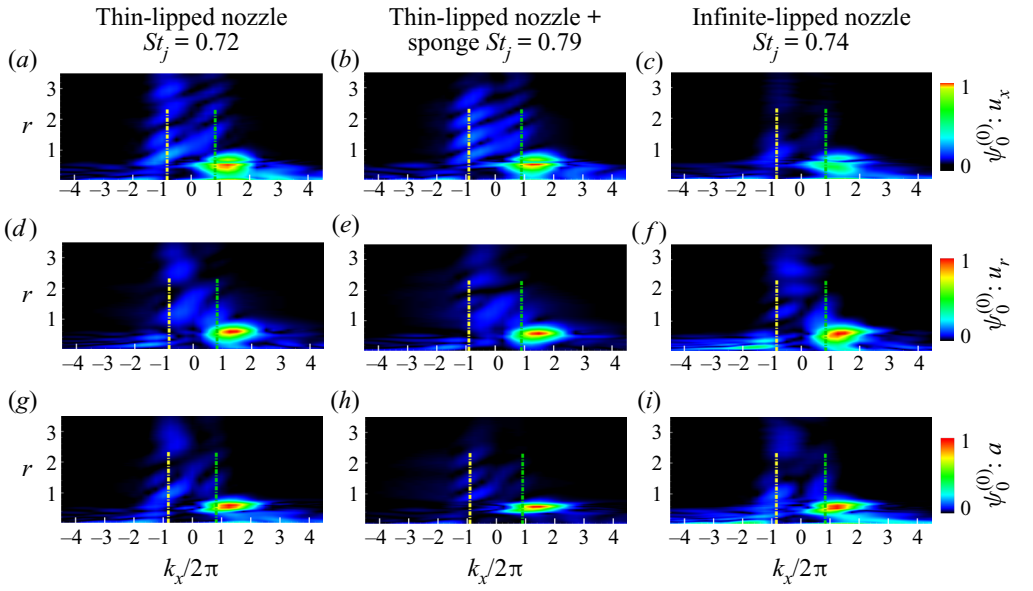



Figure 8. Streamwise and radial velocities and local speed of sound wavenumber spectra at the dominant frequency for three cases: thin-lipped nozzle (*a*,*d*,*g*), thin-lipped nozzle with the sponge (*b*,*e*,*h*) and infinite-lipped nozzle (*c*,*f*,*i*). The dotted green and yellow vertical lines denote the speed of sound in the upstream and downstream directions, respectively. Negative wavenumbers correspond to waves travelling in the upstream direction and positive wavenumbers correspond to waves travelling downstream.

analysis of the energy norm show multiple peaks. In addition, POD ranks modes based on their energy content, not their frequency characteristics. Therefore, SPOD is used in this study to investigate the upstream-travelling and the downstream-travelling wavepackets with more confidence, since each SPOD mode has a well-defined frequency while also being energy ranked. It is worth noting that experimental studies are limited to 2C–2D velocity fields, while the kernel of POD is the kinetic energy norm that requires three components of the velocity fields in incompressible flows and the total energy norm that requires three components of the velocity fields, as well as pressure and temperature fields in compressible flows.

Figure 8 shows the wavenumber spectra of the streamwise and radial-velocity components, as well as the local speed of sound at the dominant frequency for three cases of the thin-lipped nozzle (*a*,*d*,*g*), the thin-lipped nozzle with the sponge region (*b*,*e*,*h*) and the infinite-lipped nozzle (*c*,*f*,*i*). The dotted green and yellow vertical lines denote the speed of sound in the upstream and downstream directions, respectively. It should be noted that negative wavenumbers correspond to upstream-travelling waves, while positive wavenumbers correspond to downstream travelling waves. The spectra show that the wavepackets with peak amplitudes at the shear layer of the jets travel downstream with a phase velocity of approximately $0.63U_j$ and this behaviour is similar in all three cases independent of the external geometry of the nozzle. This phase speed, which is associated with the convection velocity of the coherent structures in supersonic impinging jets, is in good agreement with the previous studies listed in table 2.

There are also components with negative phase velocities in three regions: inside; the shear layer (i.e. $r/d < 0.5$); and the near field of the jets for all three cases. The upstream-travelling wavepackets are different for the different external geometry of



https://doi.org/10.1017/jfm.2021.822 Published online by Cambridge University Press

| Convection velocity | NPR | Nozzle-to-wall distance | Reference |
|---|---|---|---|
| $0.61U_j$ | 3.67 | $5d$ | Bogey & Gojon (2017) |
| $0.6U_j$ | 2.7 | various | Thurow, Samimy & Lempert (2002) |
| $0.55U_j$ | 2.5 | $5d$ | Krothapalli *et al.* (1999*a*,*b*) |
| $0.63U_j$ | 3.4 | $2d$ and $5d$ | Karami *et al.* (2020*a*) |

Table 2. Convection velocity of the coherent structures.

the nozzle. The upstream wavepackets inside the jet and in the shear layer of the jets are weakened when the sponge is added to the thin-lipped nozzle, whereas they are amplified in the case of the infinite-lipped nozzle. The upstream acoustic waves in the near field of the jets are also affected by the external geometry of the nozzle.

The amplitudes of upstream-travelling and downstream-travelling waves are obtained by separating the wavepackets into positive and negative phase velocities and performing an inverse fast Fourier transform. Figure 9 shows the amplitude, which resembles the envelope of wavepackets, of the downstream-travelling and upstream-travelling components of the coherent local speed of sound fluctuations determined from the optimal SPOD mode, with all values normalised by the respective maximum downstream-travelling component. In all three cases, the downstream travelling waves associated with the K–H instabilities are the strongest wavepackets. There are also strong downstream travelling wavepackets after the Mach disk that are significantly weaker than the K–H wavepackets in the thin-lipped nozzle with the sponge region case, as shown in figure 9(*a–c*). Figure 9(*d–f*) shows the contour maps of the local speed of sound amplitudes of the upstream-travelling wavepackets. The influence of the external geometry of the nozzle is clearly noticeable in these contour maps; the amplitudes are significantly different among all three cases. These upstream-travelling wavepackets can be classified as the waves inside the jet core, in the shear layer (i.e. the oblique shock–shear layer interaction) and outside of the jet. For the cases with the thin-lipped and infinite-lipped nozzles, the amplitudes of the upstream-travelling wavepackets is strong inside the jet. Conversely, these upstream-travelling wavepackets are weak in the thin-lipped nozzle with the sponge region. These waves cannot reach the internal region of the nozzle since the barrel shock, shown in figure 9 with a solid-white line, at the nozzle exit acts as a protective shield. However, they can approach the nozzle lip by travelling obliquely, with one side of the wavefront crawling on the reflected shock and the other side of the wavefront guided by the shear layer. Hence, this class of wave also contributes to closing the feedback loop. The upstream-travelling waves formed at the oblique shock–shear layer interaction are much weaker than those formed in the jet's core in all three cases. The upstream-travelling waves outside the jets are acoustic wavepackets as the vorticity is negligible in this region of the jets. They are formed near the impingement wall and their characteristics, such as the amplitude and orientation, are influenced by the external geometry of the nozzle. While previous experimental and numerical studies of impinging jets (Poldervaart & Wijnands 1974; Gojon, Bogey & Marsden 2015, 2016; Gojon & Bogey 2017; Weightman *et al.* 2017; Edgington-Mitchell 2019) reported the formation of acoustic waves at the impingement region, to the best of the authors' knowledge, this study is the first that clearly shows the influence of the nozzle's external geometry on their source location.

The real components of the local speed of sound at the leading SPOD modes – $St_j = 0.72$ for the thin-lipped nozzle case, $St_j = 0.79$ for the thin-lipped nozzle with sponge



https://doi.org/10.1017/jfm.2021.822 Published online by Cambridge University Press

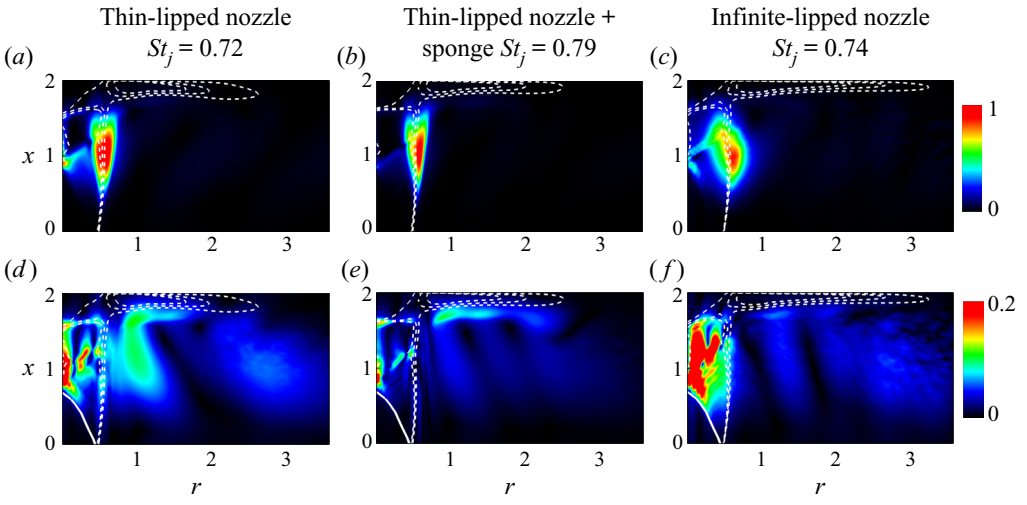



Figure 9. Amplitude of the local speed of sound fluctuations decomposed into the downstream-travelling (*a–c*) and upstream-travelling (*d–f*) components determined from the leading SPOD mode. All values are normalised with respect to the maximum downstream-travelling component. The dashed white lines are the isocontours of the non-dimensionalised mean velocity magnitude of 0.2, and the solid-white line is the intercepting, or barrel, shock.

case and $St_j = 0.74$ for the infinite-lipped nozzle case – are decomposed into components with positive and negative phase velocities to further investigate the characteristics of upstream-travelling and downstream-travelling waves. The spatial distribution of the upstream-travelling and downstream-travelling wavepackets at these SPOD modes are presented in figure 10 for the thin-lipped nozzle (*a*,*d*), the thin-lipped nozzle with the sponge (*b*,*e*) and the infinite-lipped nozzle (*c*,*f*). The downstream-travelling waves are easily identified in these figures, especially the K–H instabilities. The downstream-travelling wavepackets in the shear layer have their tails at the Mach disk and their heads at the shear layer. This connection indicates that the wavepackets at the shear layer and the Mach disk are strongly connected. Figure 10(*b*) shows that the amplitudes of the wavepackets at and after the Mach disk have decreased significantly as the sponge is integrated into the thin-lipped nozzle. Conversely, figure 10(*c*) shows an increase in the amplitudes of the downstream wavepackets at and after the Mach disk location in the infinite-lipped nozzle case.

The analysis presented in this section reveals that the upstream-travelling wavepackets exist in three regions: inside; shear layer; and outside the jets at the optimal modes. The approximate average location of the barrel shock is shown with a solid-white curve in figure 10(*d–f*) and appears as a shield at the nozzle exit. It prevents the penetration of upstream-travelling waves into the internal region of the nozzle. These contour maps also show that the spatial pattern of the upstream wavepackets outside the jets are influenced by the external geometry of the nozzle. These observation are further considered in § 4.5 using a linear impulse response analysis.

### 4.4. *Upstream-travelling waves at discrete frequencies and their nature in the receptivity process at the nozzle lip*

The decomposition analysis presented in § 4.3 suggests that further exploration of the upstream-travelling wavepackets of the optimal modes is necessary to identify



https://doi.org/10.1017/jfm.2021.822 Published online by Cambridge University Press

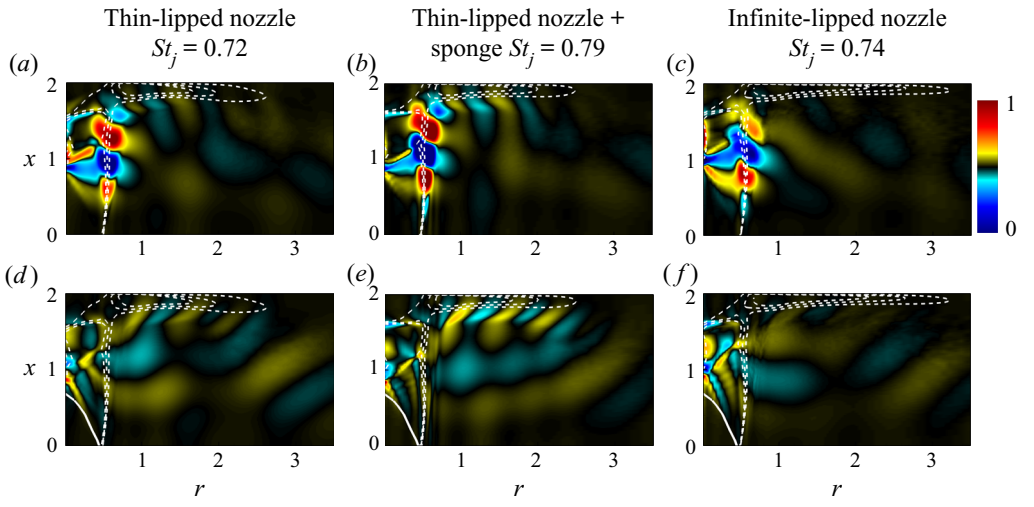



Figure 10. The local speed of sound at the leading SPOD mode decomposed into the components with positive (*a–c*) and negative (*d–f*) phase velocity for the thin-lipped nozzle (*a*,*d*), thin-lipped nozzle with the sponge (*b*,*e*) and infinite-lipped nozzle (*c*,*f*). The dashed lines are the isocontours of the non-dimensionalised mean velocity magnitude of 0.2 and the solid line is the intercepting, or barrel, shock.

their contribution to the receptivity process in this configuration. Different paths for the upstream-travelling and downstream-travelling wavepackets that contribute to the feedback loop were proposed by Weightman *et al.* (2019) based on the POD analysis of 2C–2D velocity measurements. However, in this study, we analyse the paths of the upstream-travelling wavepackets based on a more rigorous methodology using the SPOD method. As highlighted, the SPOD approach leads to spatial modes that each have a well-defined frequency. The decomposition of these spatial modes into the upstream-travelling and downstream-travelling waves suggests new upstream-travelling paths, presented schematically in figure 11.

Figure 9(*d–f*) demonstrate that the dominant acoustic waves with the potential to reach the nozzle lip and close the feedback loop belong to three types of wavepackets located in the jet's core, the jet's shear layer and outside the periphery of the jet. Therefore, assuming that the location of the acoustic source corresponding to the mode of interest is given as indicated by the red circles in figure 11, an upstream-travelling acoustic wave has three possible paths to reach the nozzle lip without being reflected by a reflective surface. For the upstream-propagating waves with the source location outside the jet, these paths are: (I) a direct path from the source to the nozzle lip; (II) an upstream free acoustic wave that travels in the shear layer; and (III) an upstream free acoustic wave that travels in the jet core. The latter appears as an obliquely travelling wave with one side of the wavefront crawling on the reflected shock, while the other side of the wavefront is guided by the shear layer of the jet. For the upstream-propagating waves with the source located at the jet's shear layer, the possible paths are: (II) a direct path from the source created at the shear layer to the nozzle lip; and (III) an upstream obliquely travelling wave that crawls on the reflected shock. For the upstream-propagating waves with the source located at the jet's core, these paths are: (II) an upstream acoustic wave that travels in the shear layer; and (III) an upstream acoustic wave crawling on the reflected shock that is formed at the interaction of the reflected shock and the shear layer. The other plausible path is a direct reflection from a reflective surface, path (IV) in figure 11. The proposed upstream-travelling paths in



https://doi.org/10.1017/jfm.2021.822 Published online by Cambridge University Press

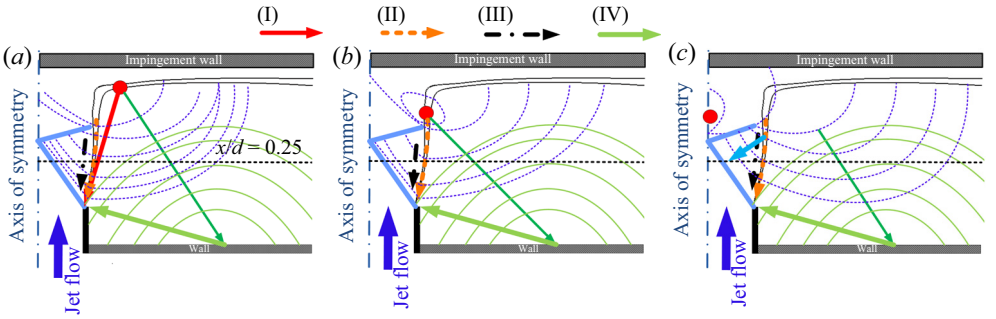



Figure 11. Proposed paths of the travelling aeroacoustic waves that contribute to the feedback loop as the origin of the upstream acoustic wavepackets changes. The barrel and reflected shocks are shown schematically with solid blue lines. The propagation direction of the wavefront that is crawling on the reflected shock on one side and is guided by the shear layer on the other side is marked with a solid cyan arrow.

this study can be considered as an extension to the proposed aeroacoustic feedback paths of Weightman *et al.* (2019) by expanding their acoustic path 1 into three separate paths.

The radial profiles of the amplitude of the upstream-travelling and downstream-travelling waves at $x/d = 0.25$ are examined to study the contribution of wavepackets at the optimal and suboptimal frequencies in the receptivity process. This axial location, as demonstrated schematically in figure 11 with a black horizontal line, allows the amplitude of the upstream-travelling waves associated with paths (I), (II) and (III) to be distinguished. It is worth noting that farther upstream, near the nozzle, the two paths of (I) and (II) merge due to the expansion of the shear layer in the configuration of this study.

Figure 12 shows the radial profiles of the upstream-travelling waves at the optimal and suboptimal frequencies at the axial location of $x/d = 0.25$ for the three cases under investigation. The amplitudes in these profiles are normalised with respect to the maximum amplitude of the downstream travelling wave for each case.

Starting with the thin-lipped nozzle case, the amplitude of the upstream-travelling waves in the shear layer and periphery of the jet (i.e. $0.3 < r/d < 0.7$) are the largest at the optimal mode ($St_j = 0.72$). This indicates that the dominant upstream-travelling wave in this configuration at the optimal mode travels along paths (I) and (II). The near field upstream-travelling wave (i.e. in the region of $r/d > 0.75$) is clearly noticeable at this frequency, which indicates the presence of waves that travel upstream from an acoustic source location with a pattern, as shown by the blue dashed curves in figure 11. However, the suboptimal mode (i.e. $St_j = 0.58$) shows large amplitudes of upstream-travelling waves both inside (in the region of $0.2 < r/d < 0.5$) and outside (in the region of $0.6 < r/d < 0.75$) the jet. Hence, at suboptimal mode $St_j = 0.58$, the upstream-travelling waves travel on paths (I) and (III).

Figure 12(*b*) shows the upstream-travelling waves at the optimal and suboptimal frequencies for the thin-lipped nozzle with the sponge region. The optimal mode ($St_j = 0.79$) has the largest amplitude of the upstream-travelling waves in the shear layer and the periphery of the jet, with peaks at $r/d = 0.5$ and 0.58; hence, the upstream-travelling waves at the optimal mode travel on paths (I) and (II) – similar to the thin-lipped nozzle. The near field upstream-travelling wave (in the region of $r/d > 0.75$) is weaker than that of the thin-lipped nozzle, indicating that the sponge weakens the upstream-travelling waves in this case. However, the suboptimal, low-frequency mode ($St_j = 0.15$) shows a large amplitude of an upstream-travelling wave outside the jet (in the region of $0.6 < r/d < 0.75$); hence, the upstream-travelling wave travels on path (I) at this frequency.



https://doi.org/10.1017/jfm.2021.822 Published online by Cambridge University Press

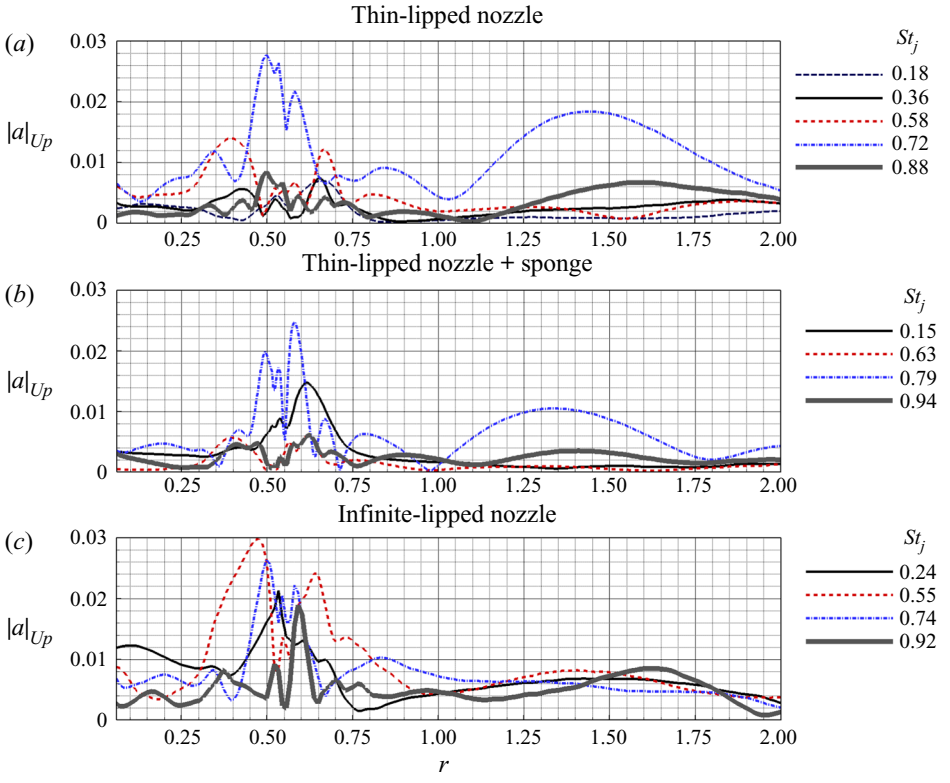



Figure 12. Radial distribution of the upstream-travelling waves (the local speed of sound component) at optimal and suboptimal frequencies and at $x/d = 0.25$ for the thin-lipped nozzle (*a*), the thin-lipped nozzle with the sponge (*b*) and the infinite-lipped nozzle (*c*).

For the infinite-lipped nozzle case, the upstream-travelling waves of the optimal and suboptimal frequencies contribute nearly equally to the process – the amplitudes are approximately equal at optimal and suboptimal frequencies but they travel on different paths. The low-frequency mode ($St_j = 0.24$) has a maximum amplitude of the upstream-travelling wave in the shear layer, while the high-frequency mode ($St_j = 0.92$) has a maximum amplitude of the upstream-travelling wave outside the jet (in the region of $0.6 < r/d < 0.7$). However, the two other frequencies have large amplitudes of upstream-travelling waves inside the jet, at the shear layer and at the periphery of the jet (in the region of $0.3 < r/d < 0.7$). Therefore, the low-frequency wave ($St_j = 0.24$) travels on path (II), the high-frequency wave ($St_j = 0.92$) travels on path (III) and the two other frequencies travel on paths (I), (II) and (III). The near field upstream-travelling wave (in the region of $r/d > 0.75$) is weaker than that of the upstream-travelling wave in the two other cases, which is probably because the waves are reflected by the infinite-lipped nozzle.

The last acoustic path – path (V) shown with a green arrow in figure 11 – is indeed a downstream-travelling wave. This downstream-travelling wave is the consequence of the reflective surface. The wavefronts of this downstream-travelling wave are shown schematically as light-green curves in figure 11. Figure 13 shows the radial profiles of the amplitudes of the local speed of sound that travel downstream at at $x/d = 0.25$ (i.e. the same axial location as in figure 12).

Figure 13(*a*) shows the radial profiles of the downstream-travelling waves at the axial location of $x/d = 0.25$ and for the optimal and suboptimal frequencies of the thin-lipped



https://doi.org/10.1017/jfm.2021.822 Published online by Cambridge University Press

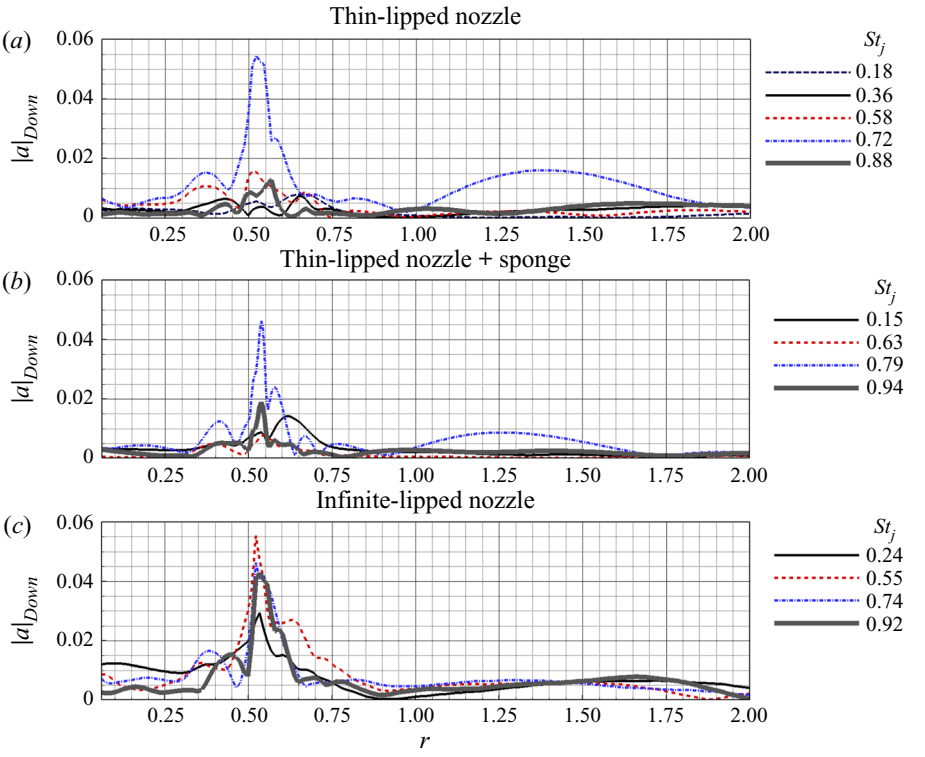



Figure 13. Radial distribution of the downstream-travelling waves (the local speed of sound component) at optimal and suboptimal frequencies at $x/d = 0.25$ for the thin-lipped nozzle ($a$), thin-lipped nozzle with the sponge ($b$) and infinite-lipped nozzle ($c$).

nozzle case, with all amplitudes normalised by the respective maximum amplitude of the downstream-travelling wave. The amplitude of the downstream-travelling waves at the optimal SPOD mode is maximal at the shear layer as expected – that is, the K–H instabilities are dominant in the shear layer. The near field wave in the $r/d > 1.0$ region is also strong, indicating strong reflective waves by the wall attached to the root of the nozzle in this configuration. At the suboptimal SPOD modes, the downstream-travelling waves are negligible compared with the optimal SPOD mode.

Figure 13($b$) shows the radial profiles of the downstream travelling waves at the optimal and suboptimal SPOD modes in the same axial location as in figure 13($a$) for the thin-lipped nozzle with the sponge region case. The optimal SPOD mode has a maximum amplitude in the shear-layer region, while the SPOD mode with a low Strouhal number ($St_j = 0.15$) has an amplitude peak in the periphery of the jet. The near field wave in the $r/d > 1.0$ region is weak because the sponge region weakens the reflection from the wall attached to the root of the nozzle.

The behaviour is completely different in the infinite-lipped nozzle case (figure 13$c$). Optimal and suboptimal SPOD modes are all active in both the shear layer and the periphery of the jet. The near field wave in the $r/d > 1.0$ region is active at all SPOD modes, with an amplitude weaker than the optimal mode of the thin-lipped nozzle case and a similar amplitude to the optimal mode of the thin-lipped nozzle with the sponge case. It appears that the sponge suppresses the near field wavepackets, and the wavepacket at the optimal mode is squeezed into the shear-layer region, while the infinite-lipped nozzle leads



https://doi.org/10.1017/jfm.2021.822 Published online by Cambridge University Press

to a more complex behaviour by distributing the energy approximately equally between the optimal and suboptimal SPOD modes.

### 4.5. *Impulse response analysis and the travelling paths of wavepackets*

Impulse response analysis is performed to further clarify the proposed paths of the wavepackets contributing to the feedback loop mechanism as presented in § 4.4 and summarised in figure 11.

A brief summary of the mathematical framework of the analysis is presented here with the interested reader referred to Karami *et al.* (2018*b*, 2020*b*) for a more detailed exposition. The linearised compressible Navier–Stokes equations (LNSE) are derived by superimposing small-amplitude disturbances onto a mean flow field. The three-dimensional LNSE are given in the concise matrix form as

$$\frac{\partial q'}{\partial t} = \mathbb{A}q', \tag{4.1}$$

where $q'$ is the perturbations of primitive variables $(\rho', u'_x, u'_r, u'_\theta, e')$ and $\mathbb{A}$ is the linear operator advancing the small perturbation in time.

An acoustic impulse described by

$$p'(t=0) = B\exp\left(-\frac{(x-x_o)^2}{2\sigma_x^2} - \frac{(r-r_o)^2}{2\sigma_r^2}\right)\cos(2\pi m\theta) \tag{4.2}$$

is used as a localised initial condition of the acoustic irrotational pressure fluctuations, where '$B$' is the amplitude of the impulse; $x_o$ and $r_o$ are the streamwise and radial location of the centre of the impulse, respectively; $\sigma_x$ and $\sigma_r$ are the radii of the impulse in the streamwise and radial directions, respectively, with $\sigma_x$ and $\sigma_r \ll \lambda$ the acoustic wavelength; and $m$ is the azimuthal mode number. In this study, '$B$' is 0.01, $\sigma_x = \sigma_r = 0.05$ and $m = 0$. The centre of the impulse is located at a radius of $R_p$ from the nozzle lip and an angle of $\theta_p$, where $\theta_p$ is the angle from the jet shear line. This corresponds to the location of the impulse in the axial and the radial directions of $x_o = R_p\sin(\theta_p)$ and $r_o = R_p\cos(\theta_p)$. Three angular positions of $-20$ (centreline of the jet), 0 (shear layer) and 45 (near field) are considered to investigate the scenarios presented in figure 11. Four cases are simulated. In the first three cases, the impulse radial location ($R_p$) is fixed at 1.2 and the angular location changes. In the last case, the angular location is $-20$, but the radial location is reduced to 0.8. This last case is simulated to explore path (III) in figure 11.

The objective of this analysis is to clarify the proposed paths of the travelling waves that contribute to the receptivity process as schematically presented in figure 11. Therefore, the analysis in this demonstration is limited to the thin-lipped nozzle case. Using the mean flow fields obtained from the ensemble average of the LES results, the three-dimensional LNSE are solved with the same LES resolution in a smaller domain in the radial direction (i.e. 4.9 in the radial direction). A sixth-order central finite difference method and a fourth-order, five-step Runge–Kutta are used for the spatial discretisation and temporal integration, respectively (Karami *et al.* 2020*b*).

The time evolution of the perturbations of the total energy for the cases with the impulse located at $\theta_p = -20^\circ$ with $R_p = 1.2$ (centreline), $\theta_p = 0^\circ$ with $R_p = 1.2$ (hear layer), $\theta_p = -45^\circ$ with $R_p = 1.2$ (near field) and $\theta_p = -20^\circ$ with $R_p = 0.8$ are presented from left to right in figure 14. The white isolines mark the local ensemble-averaged streamwise velocity equal to the speed of sound. The sequential two-dimensional snapshots ($x$–$r$ plane at azimuthal location of $\theta = 0$) are presented for the instants of $t_0$ to $t_7$ with the time difference of 0.5 acoustic time units between the snapshots.



https://doi.org/10.1017/jfm.2021.822 Published online by Cambridge University Press

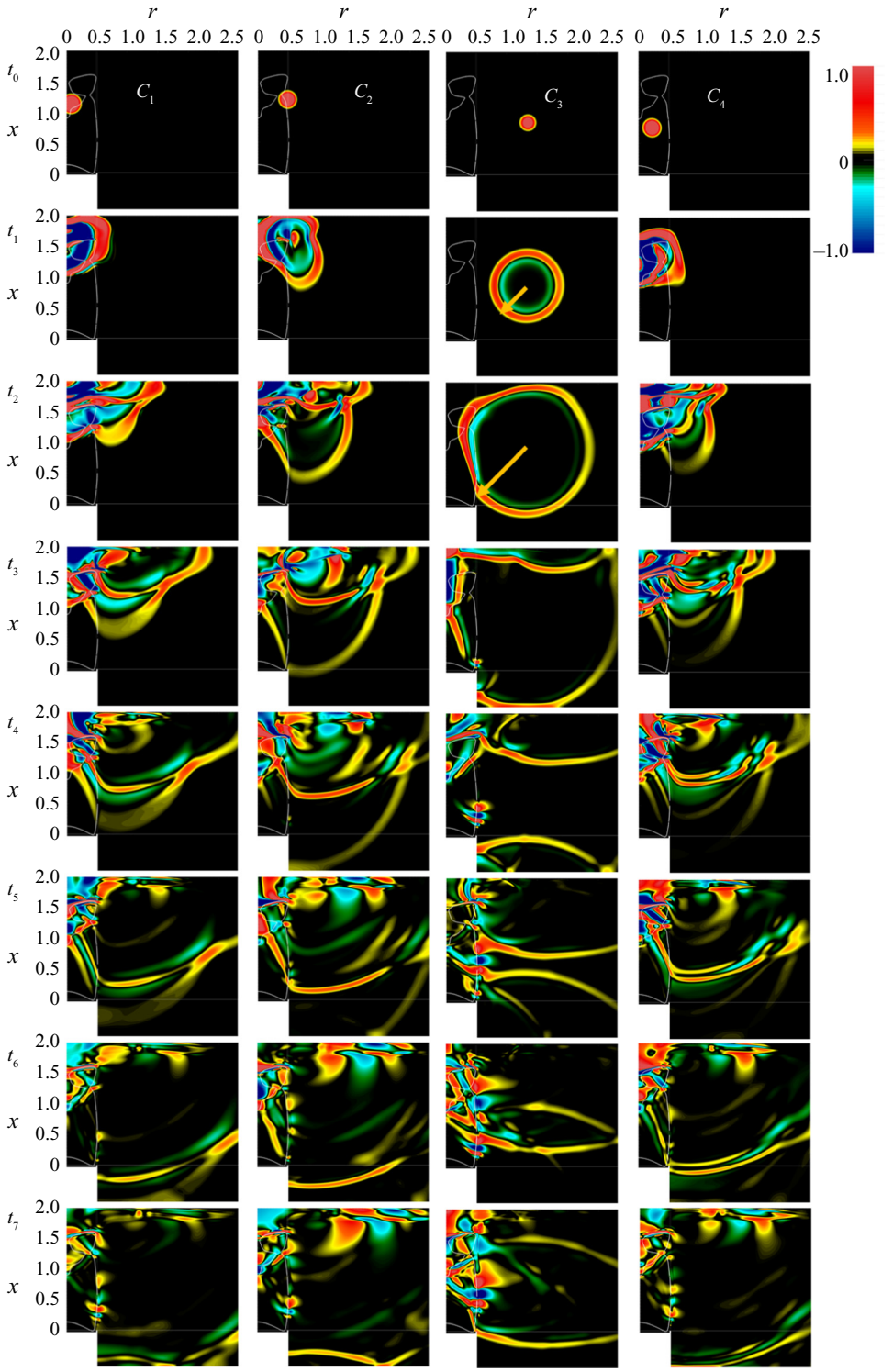



Figure 14. Instantaneous contours of the total energy fluctuation fields of the pressure impulse simulations for the impulses located at $(R_p, \theta_p)$ of (1.2, −20°) for case $C_1$, at (1.2, 0°) for case $C_2$, at (1.2, 45°) for case $C_3$ and at (0.8, −20°) for case $C_4$.



https://doi.org/10.1017/jfm.2021.822 Published online by Cambridge University Press

For cases $C_1$, $C_2$ and $C_4$, the impulse is located in or near the supersonic region; hence, the travelling wave cannot travel upstream in the streamwise direction, as can be observed in these snapshots. However, they eventually go around this obstacle (reflected shock) and travel upstream obliquely, as can be observed in instances $t_1$ to $t_4$ for $C_1$, $C_2$ and $C_4$. In the time series presented in figure 14 and the animations provided as supplementary materials, this group of wavepackets travels inside the jet. These wavepackets crawl on the reflected shock on one side and are guided by the shear layer on the other side. They reach the barrel shock and eventually disappear. They cannot penetrate the supersonic region, as the flow velocity normal to the wavefront is larger than the speed of sound; however, the wavefront guided by the shear layer can reach the nozzle lip from inside the jet. This path of the travelling wave is path (III) in the proposed paths of the upstream-travelling waves in figure 11. The same spatial distributions of wavepackets were observed in the speed of sound component of the optimal upstream-travelling waves in LES results in figure 10(*d–f*).

The near field acoustic waves travelling in a direct path towards the nozzle lip (i.e. the path (I) in figure 11) are easy to retrieve from time instances of $t_1$ to $t_4$ for the case $C_3$, as shown with an orange arrow in figure 14. At instance $t_3$ of case $C_3$, it is also clearly observable that paths (I) and (II) merge as the wavefront approaches the nozzle lip.

Paths (II) and (IV) are clearly noticeable in the time history presented in figure 14 for all four cases. wavepackets travel upstream on the shear layer on path (II), and near field wavepackets reflected by the plate attached to the root of the nozzle travel downstream on path (IV).

## 5. Discussion and conclusion

The role of the nozzle's external geometry on the upstream-travelling wavepackets in the configuration of under-expanded supersonic impinging jets is studied for three nozzle configurations using temporally resolved LES.

The ensemble-averaged analysis shows that the changes in the nozzle's external geometry significantly modify the first-order statistics. It also shows that the recirculation zone in the impingement region presents in the thin-lipped and infinite-lipped nozzle cases, while it nearly disappears in the thin-lipped nozzle with the sponge case.

Spectral proper orthogonal decomposition, as a rigorous method compared with space-only POD, is used to obtain the spatial modes that each has a single frequency characteristic. Eigenvalue spectra of the first three azimuthal mode numbers reveal multiple peaks at discrete frequencies at the axisymmetric mode ($m = 0$) for the three cases in this study. It is also observed from the eigenvalue spectra that the optimal modes of the thin-lipped nozzle and the thin-lipped nozzle with the sponge are an order of magnitude stronger than the suboptimal modes while the optimal and suboptimal modes of the infinite-lipped nozzle have comparable amplitudes. Finally, it is observed that the Strouhal number of the optimal SPOD modes undergo a minor shift as the nozzle's external geometry is modified. The spatial distributions of the low-frequency modes of all three cases show strong wavepackets in the wall jet region.

The spatial evolution of the leading SPOD modes at the optimal and suboptimal frequencies are isolated into the upstream-travelling (negative phase velocity) and downstream-travelling (positive phase velocity) wavepackets by bandpass filtering. The amplitude of the downstream wavepackets (indicating the wavepacket envelope) that resemble K–H instabilities are dominant in the shear layer. Downstream-travelling



https://doi.org/10.1017/jfm.2021.822 Published online by Cambridge University Press

wavepackets also appear after the Mach disk at optimal SPOD modes. The upstream-travelling wavepackets are active in the three regions of the inside, shear layer and near field of the jets. The amplitudes of the upstream-travelling waves are weakened by the sponge being added to the thin-lipped nozzle. Conversely, an infinite-lipped nozzle results in complex behaviour with strong upstream-travelling waves inside the jet. In all three configurations of this study, due to the NPR, the barrel shock at the nozzle exit acts as a shield preventing upstream-travelling waves from reaching the internal region of the nozzle.

There are numerous paths that acoustic waves can take to reach the nozzle lip and initiate shear-layer instabilities. Based on the spatial distribution of the SPOD modes and the instantaneous density-gradient fields, several paths of the travelling aeroacoustic waves that contribute to the feedback loop are proposed. The upstream-travelling waves from the acoustic source can travel via a direct path to the lip, the shear layer and inside the jet. The upstream-travelling waves inside the jet travel obliquely with one side of the wavefront crawling on the reflected shock and the other side guided by the shear layer. This type of wavepacket travels towards the barrel shock but fails to penetrate into the internal region of the nozzle, as the local velocity normal to the propagation direction is higher than the speed of sound. Downstream-travelling waves reflected by reflective surfaces, i.e. the perfectly reflecting surface attached to the root of the nozzle in the thin-lipped nozzle case, the imperfect acoustic absorption surface that cannot suppress all acoustic waves in the thin-lipped nozzle with the sponge case and the infinite-lipped nozzle case, also contribute to closing the feedback loop.

The isolated upstream-travelling and downstream-travelling waves at the optimal and suboptimal SPOD modes are used to evaluate the proposed paths. The results show that the optimal SPOD mode has the highest amplitude of upstream-travelling waves in the shear layer for the thin-lipped nozzle and thin-lipped nozzle with the sponge cases. In the thin-lipped nozzle case, the suboptimal SPOD mode with a Strouhal number of 0.58 has high-amplitude upstream-travelling waves inside the jet and also outside the periphery of the jet. In contrast, the suboptimal SPOD mode (Strouhal number of 0.15) of the thin-lipped nozzle with the sponge case has a high-amplitude upstream-travelling wave outside the jet's shear layer. In contrast, the results of the infinite-lipped nozzle case show that all SPOD modes have high-amplitude upstream-travelling waves that are active in all three regions: inside the jet; in the shear layer; and outside the jet. A complementary impulse response analysis was also performed that clarifies the proposed acoustic paths.

The present study shows that acoustic waves that contribute to the receptivity process have different frequencies and select different paths to reach the nozzle in ways that are sensitive to the external geometry of the nozzle. The findings that upstream-travelling waves at discrete frequencies have high amplitudes at different regions of the jets and depend on both the frequency and external geometry of the nozzle is significant in the understanding of the feedback loop phenomenon.

**Supplementary movies.** Supplementary movies are available at https://doi.org/10.1017/jfm.2021.822.

**Acknowledgements.** The research benefited from computational resources provided through the National Computational Merit Allocation Scheme, supported by the Australian Government. The computational facilities supporting this project included the Australian NCI Facility, the partner share of the NCI facility provided by Monash University through a ARC LIEF grant and the Multi-modal Australian ScienceS Imaging and Visualisation Environment (MASSIVE).

**Funding.** This work was supported by the Australian Research Council through the Discovery Project scheme: DP160102833.



https://doi.org/10.1017/jfm.2021.822 Published online by Cambridge University Press

**Declaration of interests.** The authors report no conflict of interest.

**Author ORCIDs.**
Shahram Karami https://orcid.org/0000-0003-0254-4733;
Julio Soria https://orcid.org/0000-0002-7089-9686.

## References

ALMGREN, A.S., BELL, J.B., NONAKA, A. & ZINGALE, M. 2008 Low mach number modeling of type Ia supernovae. III. Reactions. *Astrophys. J.* **684** (1), 449.

ALVI, F.S., SHIH, C., ELAVARASAN, R., GARG, G. & KROTHAPALLI, A. 2003 Control of supersonic impinging jet flows using supersonic microjets. *AIAA J.* **41** (7), 1347–1355.

AMILI, O., EDGINGTON-MITCHELL, D., HONNERY, D. & SORIA, J. 2015*a* High resolution PIV measurements of an impinging underexpanded supersonic jet. In *Turbulence and Shear Flow Phenomena* (ed. S. Tavoularis & I. Marusic), *June 30–July 3, University of Melbourne, Melbourne, Australia*.

AMILI, O., EDGINGTON-MITCHELL, D., WEIGHTMAN, J., STEGEMAN, P., OOI, A., HONNERY, D. & SORIA, J. 2015*b* PIV measurement of an impinging underexpanded supersonic jet and comparison with LES. In *11th International Symposium on Particle Image Velocimetry, September 14–16, Santa Barbara, California, USA*.

AMJAD, S., KARAMI, S., SORIA, J. & ATKINSON, C.H. 2020 Assessment of three-dimensional density measurements from tomographic background-oriented schlieren (BOS). *Meas. Sci. Technol.* **31** (11), 114002.

BAGHERI, S., SCHLATTER, P., SCHMID, P.J. & HENNINGSON, D.S. 2009 Global stability of a jet in crossflow. *J. Fluid Mech.* **624**, 33–44.

BENDAT, J.S. & PIERSOL, A.G. 1966 *Measurement and Analysis of Random Data*. Wiley.

BODONY, D.J. 2006 Analysis of sponge zones for computational fluid mechanics. *J. Comput. Phys.* **212** (2), 681–702.

BODONY, D.J. & LELE, S.K. 2005 On using large-eddy simulation for the prediction of noise from cold and heated turbulent jets. *Phys. Fluids* **17** (8), 085103.

BOGEY, C. & GOJON, R. 2017 Feedback loop and upwind-propagating waves in ideally expanded supersonic impinging round jets. *J. Fluid Mech.* **823**, 562–591.

BOGEY, C., MARSDEN, O. & BAILLY, C. 2011 Large-eddy simulation of the flow and acoustic fields of a Reynolds number $10^5$ subsonic jet with tripped exit boundary layers. *Phys. Fluids* **23** (3), 035104.

BRÈS, G., JORDAN, P., JAUNET, V., LE RALLIC, M., CAVALIERI, A., TOWNE, A., LELE, S., COLONIUS, T. & SCHMIDT, O. 2018 Importance of the nozzle-exit boundary-layer state in subsonic turbulent jets. *J. Fluid Mech.* **851**, 83–124.

CITRINITI, J.H. & GEORGE, W.K. 2000 Reconstruction of the global velocity field in the axisymmetric mixing layer utilizing the proper orthogonal decomposition. *J. Fluid Mech.* **418**, 137–166.

COLONIUS, T. & LELE, S.K. 2004 Computational aeroacoustics: progress on nonlinear problems of sound generation. *Prog. Aerosp. Sci.* **40** (6), 345–416.

COLONIUS, T., LELE, S.K. & MOIN, P. 1997 Sound generation in a mixing layer. *J. Fluid Mech.* **330**, 375–409.

DAUPTAIN, A., CUENOT, B. & GICQUEL, L.Y.M. 2010 Large eddy simulation of stable supersonic jet impinging on flat plate. *AIAA J.* **48** (10), 2325–2338.

DAUPTAIN, A., GICQUEL, L.Y.M. & MOREAU, S. 2012 Large eddy simulation of supersonic impinging jets. *AIAA J.* **50** (7), 1560–1574.

DAVIDSON, L. 2009 Large eddy simulations: how to evaluate resolution. *Intl J. Heat Fluid Flow* **30** (5), 1016–1025.

DELVILLE, J., UKEILEY, L., CORDIER, L., BONNET, J.-P. & GLAUSER, M. 1999 Examination of large-scale structures in a turbulent plane mixing layer. Part 1. Proper orthogonal decomposition. *J. Fluid Mech.* **391**, 91–122.

DONALDSON, C. & SNEDEKER, R.S. 1971 A study of free jet impingement. Part 1. Mean properties of free and impinging jets. *J. Fluid Mech.* **45** (2), 281–319.

EDGINGTON-MITCHELL, D. 2019 Aeroacoustic resonance and self-excitation in screeching and impinging supersonic jets–a review. *Intl J. Aeroacoust.* **18** (2–3), 118–188.

EDGINGTON-MITCHELL, D., HONNERY, D.R. & SORIA, J. 2014 The underexpanded jet mach disk and its associated shear layer. *Phys. Fluids* **26** (9), 1578.

EDGINGTON-MITCHELL, D., JAUNET, V., JORDAN, P., TOWNE, A., SORIA, J. & HONNERY, D. 2018 Upstream-travelling acoustic jet modes as a closure mechanism for screech. *J. Fluid Mech.* **855**, R1.



https://doi.org/10.1017/jfm.2021.822 Published online by Cambridge University Press

EDGINGTON-MITCHELL, D., WANG, T., NOGUEIRA, P., SCHMIDT, O., JAUNET, V., DUKE, D., JORDAN, P. & TOWNE, A. 2021 Waves in screeching jets. *J. Fluid Mech.* **913**, A7.

FREUND, J. & COLONIUS, T. 2002 POD analysis of sound generation by a turbulent jet. In *40th AIAA Aerospace Sciences Meeting and Exhibit 2002*. AIAA.

FUKAGATA, K. & KASAGI, N. 2002 Highly energy-conservative finite difference method for the cylindrical coordinate system. *J. Comput. Phys.* **181** (2), 478–498.

GAITONDE, D.V. & SAMIMY, M. 2011 Coherent structures in plasma-actuator controlled supersonic jets: axisymmetric and mixed azimuthal modes. *Phys. Fluids* **23** (9), 095104.

GLAUSER, M.N., LEIB, S.J. & GEORGE, W.K. 1987 Coherent structures in the axisymmetric turbulent jet mixing layer. In *Turbulent Shear Flows 5* (ed. F. Durst, *et al.*), pp. 134–145. Springer.

GOJON, R. & BOGEY, C. 2017 Flow structure oscillations and tone production in underexpanded impinging round jets. *AIAA J.* **55** (6), 1792–1805.

GOJON, R., BOGEY, C. & MARSDEN, O. 2015 Large-eddy simulation of underexpanded round jets impinging on a flat plate 4 to 9 radii downstream from the nozzle. *AIAA Paper* 2015-2210.

GOJON, R., BOGEY, C. & MARSDEN, O. 2016 Investigation of tone generation in ideally expanded supersonic planar impinging jets using large-eddy simulation. *J. Fluid Mech.* **808**, 90–115.

GORDEYEV, S.V. & THOMAS, F.O. 2000 Coherent structure in the turbulent planar jet. Part 1. Extraction of proper orthogonal decomposition eigenmodes and their self-similarity. *J. Fluid Mech.* **414**, 145–194.

HAGHIRI, A., TALEI, M., BREAR, M.J. & HAWKES, E.R. 2018 Sound generation by turbulent premixed flames. *J. Fluid Mech.* **843**, 29–52.

HANIFI, A., SCHMID, P.J. & HENNINGSON, D.S. 1996 Transient growth in compressible boundary layer flow. *Phys. Fluids* **8** (3), 826–837.

HELLSTRÖM, L.H.O. & SMITS, A.J. 2014 The energetic motions in turbulent pipe flow. *Phys. Fluids* **26** (12), 125102.

HENDERSON, L.F. 1966 Experiments on the impingement of a supersonic jet on a flat plate. *Z. Angew. Math. Phys.* **17** (5), 553–569.

HO, C.-M. & NOSSEIR, N.S. 1981 Dynamics of an impinging jet. Part 1. The feedback phenomenon. *J. Fluid Mech.* **105**, 119–142.

KARAMI, S., EDGINGTON-MITCHELL, D. & SORIA, J. 2018*a* Large eddy simulation of supersonic under-expanded jets impinging on a flat plate. In *Proceedings of the 11th Australasian Heat and Mass Transfer Conference*, p. 12. Australasian Fluid and Thermal Engineering Society (AFTES).

KARAMI, S., EDGINGTON-MITCHELL, D., THEOFILIS, V. & SORIA, J. 2020*a* Characteristics of acoustic and hydrodynamic waves in under-expanded supersonic impinging jets. *J. Fluid Mech.* **905**, A34.

KARAMI, S. & SORIA, J. 2018 Analysis of coherent structures in an under-expanded supersonic impinging jet using spectral proper orthogonal decomposition (SPOD). *Aerospace* **5** (3), 73.

KARAMI, S., STEGEMAN, P.C., OOI, A. & SORIA, J. 2019 High-order accurate large-eddy simulations of compressible viscous flow in cylindrical coordinates. *Comput. Fluids* **191**, 104241.

KARAMI, S., STEGEMAN, P.C., OOI, A., THEOFILIS, V. & SORIA, J. 2020*b* Receptivity characteristics of under-expanded supersonic impinging jets. *J. Fluid Mech.* **889**, A27.

KARAMI, S., STEGEMAN, P.C., THEOFILIS, V., SCHMID, P.J. & SORIA, J. 2018*b* Linearised dynamics and non-modal instability analysis of an impinging under-expanded supersonic jet. In *Journal of Physics: Conference Series*, vol. 1001, p. 012019. IOP Publishing.

KAWAI, S. & LELE, S.K. 2010 Large-eddy simulation of jet mixing in supersonic crossflows. *AIAA J.* **48** (9), 2063–2083.

KENNEDY, C.A. & CARPENTER, M.H. 1994 Several new numerical methods for compressible shear-layer simulations. *Appl. Numer. Maths* **14** (4), 397–433.

KENNEDY, C.A., CARPENTER, M.H. & LEWIS, R.M. 2000 Low-storage, explicit Runge–Kutta schemes for the compressible Navier–Stokes equations. *Appl. Numer. Maths* **35** (3), 177–219.

KOSTAS, J., SORIA, J. & CHONG, M.S. 2005 A comparison between snapshot POD analysis of PIV velocity and vorticity data. *Exp. Fluids* **38** (2), 146–160.

KROTHAPALLI, A., RAJKUPERAN, E., ALVI, F. & LOURENCO, L. 1999*a* Flow field and noise characteristics of a supersonic impinging jet. *J. Fluid Mech.* **392**, 155–181.

KROTHAPALLI, A., RAJKUPERAN, E., ALVI, F. & LOURENCO, L. 1999*b* Flow field and noise characteristics of a supersonic impinging jet. In *4th AIAA/CEAS Aeroacoustics Conference*, p. 2239. AIAA.

KUMAR, R., LAZIC, S. & ALVI, F.S. 2009 Control of high-temperature supersonic impinging jets using microjets. *AIAA J.* **47** (12), 2800–2811.

LE CLAINCHE, S. & VEGA, J.M. 2017 Higher order dynamic mode decomposition to identify and extrapolate flow patterns. *Phys. Fluids* **29** (8), 084102.

LE CLAINCHE, S., VEGA, J.M. & SORIA, J. 2017 Higher order dynamic mode decomposition of noisy experimental data: the flow structure of a zero-net-mass-flux jet. *Expl Therm. Fluid Sci.* **88**, 336–353.



https://doi.org/10.1017/jfm.2021.822 Published online by Cambridge University Press

LILLY, D.K. 1992 A proposed modification of the Germano subgrid-scale closure method. *Phys. Fluids* A*: Fluid Dyn.* **4** (3), 633–635.
LIVERMORE, P.W., JONES, C.A. & WORLAND, S.J. 2007 Spectral radial basis functions for full sphere computations. *J. Comput. Phys.* **227** (2), 1209–1224.
LUMLEY, J.L. 1967 The structure of inhomogeneous turbulent flows. *Atmos. Turbul. Radio Wave Propag*. 166–177.
LUMLEY, J.L. 1981 Coherent structures in turbulence. In *Transition and Turbulence* (ed. R.E. Meyer), pp. 215–242. Academic Press.
LUMLEY, J.L. 1970 *Stochastic Tools in Turbulence*. Academic Press, New York.
MACK, L.M. 1984 Boundary-layer linear stability theory. *Tech. Rep.* ADP004046. California Inst of Tech Pasadena Jet Propulsion Lab.
MILANI, P.M., CHING, D.S., BANKO, A.J. & EATON, J.K. 2020 Shear layer of inclined jets in crossflow studied with spectral proper orthogonal decomposition and spectral transfer entropy. *Intl J. Heat Mass Transfer* **147**, 118972.
MOHSENI, K. & COLONIUS, T. 2000 Numerical treatment of polar coordinate singularities. *J. Comput. Phys.* **157** (2), 787–795.
MORINISHI, Y., VASILYEV, O.V. & OGI, T. 2004 Fully conservative finite difference scheme in cylindrical coordinates for incompressible flow simulations. *J. Comput. Phys.* **197** (2), 686–710.
NORUM, T.D. 1983 Screech suppression in supersonic jets. *AIAA J.* **21** (2), 235–240.
PAREDES, P., GOSSE, R., THEOFILIS, V. & KIMMEL, R. 2016 Linear modal instabilities of hypersonic flow over an elliptic cone. *J. Fluid Mech.* **804**, 442–466.
PELMARD, J., NORRIS, S. & FRIEDRICH, H. 2018 Les grid resolution requirements for the modelling of gravity currents. *Comput. Fluids* **174**, 256–270.
POLDERVAART, L.J. & WIJNANDS, A. 1974 Modes of vibration of an under-expanded free jet. https://www.youtube.com/watch?v=EnlCDOQW7wc.
POWELL, A. 1953 On the mechanism of choked jet noise. *Proc. Phys. Soc.* B **66** (12), 1039.
POWELL, A. 1988 The sound-producing oscillations of round underexpanded jets impinging on normal plates. *J. Acoust. Soc. Am.* **83** (2), 515–533.
PRANDTL, L. 1904 Über die stationären wellen in einem gasstrahl. *Phys. Z.* **5**, 599–6010.
RAMAN, G. & SRINIVASAN, K. 2009 The powered resonance tube: from Hartmann's discovery to current active flow control applications. *Prog. Aerosp. Sci.* **45** (4–5), 97–123.
RAY, P.K., CHEUNG, L.C. & LELE, S.K. 2009 On the growth and propagation of linear instability waves in compressible turbulent jets. *Phys. Fluids* **21** (5), 054106.
ROSSITER, J.E. 1964 Wind tunnel experiments on the flow over rectangular cavities at subsonic and transonic speeds. *Tech. Rep.* Ministry of Aviation; Royal Aircraft Establishment; RAE Farnborough.
ROWLEY, C.W. 2002 Modeling, simulation, and control of cavity flow oscillations. PhD thesis, California Institute of Technology.
SCHMID, P.J. 2010 Dynamic mode decomposition of numerical and experimental data. *J. Fluid Mech.* **656**, 5–28.
SCHMIDT, O.T. & COLONIUS, T. 2020 Guide to spectral proper orthogonal decomposition. *AIAA J.* **58** (3), 1023–1033.
SCHMIDT, O.T., TOWNE, A., RIGAS, G., COLONIUS, T. & BRÈS, G.A. 2018 Spectral analysis of jet turbulence. *J. Fluid Mech.* **855**, 953–982.
SEMLITSCH, B., MALLA, B., GUTMARK, E.J. & MIHĂESCU, M. 2020 The generation mechanism of higher screech tone harmonics in supersonic jets. *J. Fluid Mech.* **893**, A9.
SIEBER, M., PASCHEREIT, C.O. & OBERLEITHNER, K. 2016 Spectral proper orthogonal decomposition. *J. Fluid Mech.* **792**, 798–828.
SIKRORIA, T., SORIA, J., KARAMI, S., SANDBERG, R.D. & OOI, A. 2020 Measurement and analysis of the shear layer instabilities in supersonic impinging jets. In *AIAA Aviation 2020 Forum*, p. 3070. AIAA.
SIROVICH, L. 1987*a* Turbulence and the dynamics of coherent structures. I. Coherent structures. *Q. Appl. Maths* **45** (3), 561–571.
SIROVICH, L. 1987*b* Turbulence and the dynamics of coherent structures. II. symmetries and transformations. *Q. Appl. Maths* **45** (3), 573–582.
SIROVICH, L. 1987*c* Turbulence and the dynamics of coherent structures. III. dynamics and scaling. *Q. Appl. Maths* **45** (3), 583–590.
SORIA, J. & AMILI, O. 2015 Under-expanded impinging supersonic jet flow. In *10th Pacific Symposium on Flow Visualization and Image Processing* (ed. G. Cardone)*, June 15–18, Naples, Italy*.
STAHL, S.L., PRASAD, C. & GAITONDE, D.V. 2021 Distinctions between single and twin impinging jet dynamics. *J. Acoust. Soc. Am.* **150** (2), 734–744.



https://doi.org/10.1017/jfm.2021.822 Published online by Cambridge University Press

STEGEMAN, P.C., PÉREZ, J.M., SORIA, J. & THEOFILIS, V. 2016*a* Inception and evolution of coherent structures in under-expanded supersonic jets. *J. Phys.: Conf. Ser.* **708**, 012015.

STEGEMAN, P.C., SORIA, J. & OOI, A. 2016*b* Interaction of shear layer coherent structures and the stand-off shock of an under-expanded circular impinging jet. In *Fluid-Structure-Sound Interactions and Control*, pp. 241–245. Springer.

TAM, C.K.W. & AHUJA, K.K. 1990 Theoretical model of discrete tone generation by impinging jets. *J. Fluid Mech.* **214**, 67–87.

TAM, C.K.W. & DONG, Z. 1994 Wall boundary conditions for high-order finite-difference schemes in computational aeroacoustics. *Theor. Comput. Fluid Dyn.* **6** (5–6), 303–322.

THUROW, B., SAMIMY, M. & LEMPERT, W. 2002 Structure of a supersonic impinging rectangular jet via real-time optical diagnostics. In *32nd AIAA Fluid Dynamics Conference and Exhibit*, p. 2865. AIAA.

TOWNE, A., SCHMIDT, O.T. & COLONIUS, T. 2017 Spectral proper orthogonal decomposition and its relationship to dynamic mode decomposition and resolvent analysis. *J. Fluid Mech.* **825**, 1113–1152.

TOWNE, A., SCHMIDT, O.T. & COLONIUS, T. 2018 Spectral proper orthogonal decomposition and its relationship to dynamic mode decomposition and resolvent analysis. *J. Fluid Mech.* **847**, 821–867.

TUMIN, A. & RESHOTKO, E. 2003 Optimal disturbances in compressible boundary layers. *AIAA J.* **41** (12), 2357–2363.

TUTKUN, M. & GEORGE, W.K. 2017 Lumley decomposition of turbulent boundary layer at high Reynolds numbers. *Phys. Fluids* **29** (2), 020707.

TUTKUN, M., JOHANSSON, P.B.V. & GEORGE, W.K. 2008 Three-component vectorial proper orthogonal decomposition of axisymmetric wake behind a disk. *AIAA J.* **46** (5), 1118–1134.

WEIGHTMAN, J.L., AMILI, O., HONNERY, D., EDGINGTON-MITCHELL, D. & SORIA, J. 2017 On the effects of nozzle lip thickness on the azimuthal mode selection of a supersonic impinging flow. In *23rd AIAA/CEAS Aeroacoustics Conference*, p. 3031. AIAA.

WEIGHTMAN, J.L., AMILI, O., HONNERY, D., EDGINGTON-MITCHELL, D. & SORIA, J. 2019 Nozzle external geometry as a boundary condition for the azimuthal mode selection in an impinging underexpanded jet. *J. Fluid Mech.* **862**, 421–448.

WLEZIEN, R.W. & KIBENS, V. 1988 Influence of nozzle asymmetry on supersonic jets. *AIAA J.* **26** (1), 27–33.

ZAPRYAGAEV, V., KISELEV, N. & GUBANOV, D. 2018 Shock-wave structure of supersonic jet flows. *Aerospace* **5** (2), 60.

https://doi.org/10.1017/jfm.2021.822 Published online by Cambridge University Press